Full length article

Deformation mechanisms and defect structures in Heusler intermetallic MnCu$_2$Al

Bailey E. Rhodes [a], Justin A. Mayer [a], Shuozhi Xu [b], James D. Lamb [a], Joe Wendorf [a], McLean P. Echlin [a], Tresa M. Pollock [a], Yolita M. Eggeler [c], Irene J. Beyerlein [a,d,1], Daniel S. Gianola [a,*]

[a] *Materials Department, University of California, Santa Barbara, 93106, CA, USA*
[b] *School of Aerospace and Mechanical Engineering, University of Oklahoma, Norman, 73019-1052, OK, USA*
[c] *Laboratory for Electron Microscopy, Karlsruhe Institute of Technology, Karlsruhe, D-76131, Germany*
[d] *Mechanical Engineering Department, University of California, Santa Barbara, 93106, CA, USA*

ARTICLE INFO

ABSTRACT

Intermetallics with crystals derived from body-centered cubic structures are promising materials to enhance the performance and high temperature capability of high-strength alloys both as matrix materials and as strengthening precipitates. Given the ordered nature of these materials, the defect structures that ultimately mediate plasticity can be complex and strongly dependent on processing *vis-à-vis* the extent of disorder inherited from high temperature phases. Here, we elucidate the elementary characteristics of the defect structures in the Heusler ($L2_1$) intermetallic MnCu$_2$Al as investigated by the orientation-dependent strength and compressive plasticity measured from *in situ* micro-compression experiments and *post-mortem* transmission electron microscopy. Our experiments reveal single crystal compressive yield strengths as high as 1.2 GPa and a capacity for stable plastic deformation, accompanied by slip characteristics reminiscent of bcc-derived crystals. We study the equilibrium dissociation mechanisms and critical stresses of $\langle 111 \rangle \{110\}$-type dislocations in the Heusler intermetallic using an *ab initio* informed phase field dislocation dynamics model. The calculations suggest that the dislocation dissociates into multiple distinct partials, which depend on the character of the dislocation, and are closely spaced to a degree that intervening faults are undetectable using conventional transmission electron microscopy. Critical stresses to initiate glide of these defect structures quantitatively agree with measured yield strengths. Our work details the interplay between the significant degree of elastic anisotropy, stacking fault energies, and glissile defect structures governing mechanical properties and motivates an increased awareness of the role that complex defect structures play for alloy design involving bcc-derived intermetallics.

1. Introduction

Materials employed in load-bearing applications in extreme environments often contain a significant fraction of intermetallic compounds, whose capacity for dislocation-mediated plasticity is integral to the overall mechanical performance of the composite material. This trend is partially due to the design of precipitate-strengthened materials wherein the precipitate is an intermetallic phase that impedes the glide of dislocations through a metallic matrix [1–7], as well as to the rise of multi-principal element alloys and additive manufacturing, which promote increasingly diverse microstructures that include, in part, intermetallics [8–13]. Developing a strong understanding of the underlying deformation mechanisms at play within intermetallics is therefore of utmost importance.

While deformation of the $L1_2$ and $B2$ phases have received considerable attention [14–21], large gaps remain in the literature surrounding the characteristics of the defect structures, dislocation dynamics, and overall mechanical performance of several families of intermetallics that can potentially act as precipitate strengtheners. The Heusler intermetallic, which is most commonly applied in magnetic applications, is an interesting example as it is employed as a precipitate strengthener for high-strength alloys [7,12,13], yet the fundamental mechanisms governing its deformation and mechanical properties remain poorly

---

* Corresponding author.
E-mail address: gianola@ucsb.edu (D.S. Gianola).
[1] Irene J. Beyerlein was an Editor of the journal during the review period of the article. To avoid a conflict of interest, Irene J. Beyerlein was blinded to the record and another editor processed this manuscript.

understood. Specifically, the extent of stable plasticity, strength, and ductility supported in Heusler intermetallics remains unclear. The dislocation type and core structures, which significantly influence their resistance to glide through the crystal, have not yet been adequately characterized or related to plastic behavior.

Heusler intermetallics crystallize with a stoichiometry of XY_2Z in the $L2_1$ crystal structure with the $Fm\bar{3}m$ space group, and are most commonly employed in magnetic applications. They bear the name of Friedrich Heusler, the German mining engineer that discovered $MnCu_2Al$, the prototype of this material class [22]. Heusler intermetallics are generally well studied because of their multifunctional properties, including, but not limited to, their enhancement of the thermoelectric properties of half-Heusler species [23,24] and their noteworthy magneto-optical or magneto-caloric behavior, which is often enabled by a martensitic phase transformation [25]. Thus, knowledge of the mechanical properties of Heusler intermetallics is limited to those few members that act as magnetic shape memory alloys [26–35]. Though these experiments are mechanical in nature, they probe the martensitic phase transformation exhibited by these particular compositions, such that all reported strain values are representative of transformation-induced plasticity, rather than dislocation-mediated plasticity. There have, however, been several experimental reports of the slip characteristics of the prototypical Heusler intermetallic, of composition $MnCu_2Al$.

Initially $MnCu_2Al$ was described as being explosively brittle [36], but in 1977, Green et al. [37] were able to deform $MnCu_2Al$ single crystals to more than 20% shear strain, using plane-strain compression to control the applied stresses. Following deformation, Green et al. used slip trace analysis to identify the active slip planes, and $\mathbf{g}\cdot\mathbf{b}$ analysis by conventional transmission electron microscopy (TEM) to identify the slip direction of dislocations in the deformed specimen. Regardless of the initial crystalline orientation, Green et al. found that $MnCu_2Al$ deforms plastically on the $\langle 111\rangle\{110\}$ slip family. In 1984, Umakoshi et al. [38] performed experiments in uniaxial compression to identify temperature dependence in the activation of slip modes through slip trace analysis. At comparable temperatures to Green et al., Umakoshi et al. found that $MnCu_2Al$ deformed on {110} slip planes when the maximum resolved shear stress plane was {110}, but exhibited {112} slip in all other orientations [38]. The discrepancy between these results may be explained through the material processing of the specimen. In the thermal processing of their single crystalline $MnCu_2Al$ specimen, Umakoshi et al. performed mechanical testing directly after quenching from high temperatures, which differed from Green et al., who included an additional tempering step before testing the specimen. Several other studies have shown that tempering is highly impactful in reducing the number of $\langle 100\rangle\{010\}$-type antiphase boundaries (APB) formed while quenching from high temperatures, which may change the observed slip characteristics and mechanical properties [39–42]. Because of the difference in thermal processing, the observations by Umakoshi et al. and Green et al. may therefore not be comparable to one another, as they sample the effect of different processing conditions. Although there is no clear consensus as to the slip modes, all accounts agree that $MnCu_2Al$ deforms plastically with relatively high yield stresses.

Intermetallic materials commonly possess a combination of strain hardening and high yield stresses that is generally indicative of planar dislocation cores, which inhibit the glide of dislocations while maintaining plastic flow [43]. In their discussion, Green et al. predict that the combination of high strength and ductility observed in $MnCu_2Al$ may originate from the dissociation of the observed $\langle 111\rangle$ dislocations into four partial dislocations, each with the $\frac{1}{4}\langle 111\rangle$ Burgers vector, creating four antiphase boundaries *via*

$$[111] = \frac{1}{4}[111] + \frac{1}{4}[111] + \frac{1}{4}[111] + \frac{1}{4}[111] \tag{1}$$

[37]. However, micrographs of antiphase boundaries caused by plastic deformation in $MnCu_2Al$ have so far been elusive [36,40].

In this article, we investigate the deformation mechanisms and planar defect structures that are generated through compressive plastic deformation of micro-pillars of $MnCu_2Al$. Our micro-compression experiments reveal mechanical anisotropy, compressive yield strengths as high as 1.2 GPa, as well as stable compressive plasticity. We apply *post-mortem* slip trace analysis and TEM to characterize $\langle 111\rangle\{110\}$ slip characteristics that are reminiscent of bcc-derived $B2$ intermetallics. We complement these experimental findings with modeling at multiple length scales to gain insight into potential planar defects present within $MnCu_2Al$. An *ab initio* phase field dislocation dynamics (PFDD) model is designed to calculate the equilibrium structure of the dislocation cores and the minimum applied stress needed to initiate glide. Experimental elastic constants [37] and density functional theory (DFT) calculations of the lattice parameter, and full γ-surface, are the only input into the calculation.

2. Materials and methods

2.1. Material preparation

A polycrystalline ingot of $MnCu_2Al$ was prepared using a combination of arc melting and furnace annealing according to previous investigations [39–41]. Elemental Mn (Sigma Aldrich, chips, 99%) was cleaned of its native oxides by annealing in an evacuated silica ampule for 8 h at 1000 °C. Starting materials of cleaned Mn, Cu (Alfa Aesar, wire, 99.99%), and Al (Alfa Aesar, wire, 99.9995%) were weighed with a 1:2:1 stoichiometry, totaling a mass of 3.0 g. An additional excess of Mn (10 mg) was added to compensate for volatilization during melting. The materials were arc melted four times in an Ar atmosphere, flipping the ingot between melts for homogeneity, with a total mass loss of 1.3%. The resulting ingot was wrapped in Ta foil, sealed in an evacuated silica ampule, and homogenized at 850 °C for 7 days to create a large-grained microstructure, then quenched into water. To ensure structural homogeneity, the ingot was divided and pieces were sampled from opposing faces of the ingot, ground into a fine powder, and sieved through a 140 mesh (106 μm particle size) for a synchrotron powder X-ray diffraction (XRD) sample. The powder sample was again sealed within an evacuated fused silica ampule and tempered at 320 °C for 1 h to resolve any pre-existing crystallographic defects [39,44]. Microscopy and mechanical testing were performed on pieces of the ingot that were tempered under the same conditions.

2.2. Characterization

Experimental techniques including XRD, scanning electron microscopy (SEM), electron backscatter diffraction (EBSD), and TEM were applied to characterize the samples in this investigation. Synchrotron powder XRD data were collected on beam line 11-BM at the Advanced Photon Source, Argonne National Laboratory ($\lambda = 0.458944$ Å). The resulting patterns were refined using TOPAS Academic V7 [45] and plotted using the scientific color map, batlow [46]. Representations of the Heusler structure were drawn using VESTA 3 [47]. SEM was performed using either an Thermo Fisher Scientific (TFS) Apreo C SEM, TFS Apreo S SEM, or an TFS Versa 3D FIB-SEM, operating at an accelerating voltage of 10 kV and an electron beam current of 0.8 nA using secondary and backscatter electron detectors. EBSD maps were collected at an accelerating voltage of 30 kV and electron beam current of 32 nA using either an TFS Apreo C SEM or an TFS Versa 3D FIB-SEM. Scan areas of size 400 μm × 400 μm were collected with 4 × 4 binning, a 6 μm step size, and were enhanced by a background subtraction. EBSD data are visualized on the fcc IPF triangle using the MTEX 5.8 toolbox [48]. Focused ion beam (FIB) milling was performed using an TFS Helios NanoLab 600, operating at a voltage of 30 kV at various currents, and finished with a final ion polishing step at 5 kV, 16 pA to minimize FIB-induced damage. Defects were imaged using an TFS Osiris ChemiStem and TFS Titan3 80-300 S(TEM), operating
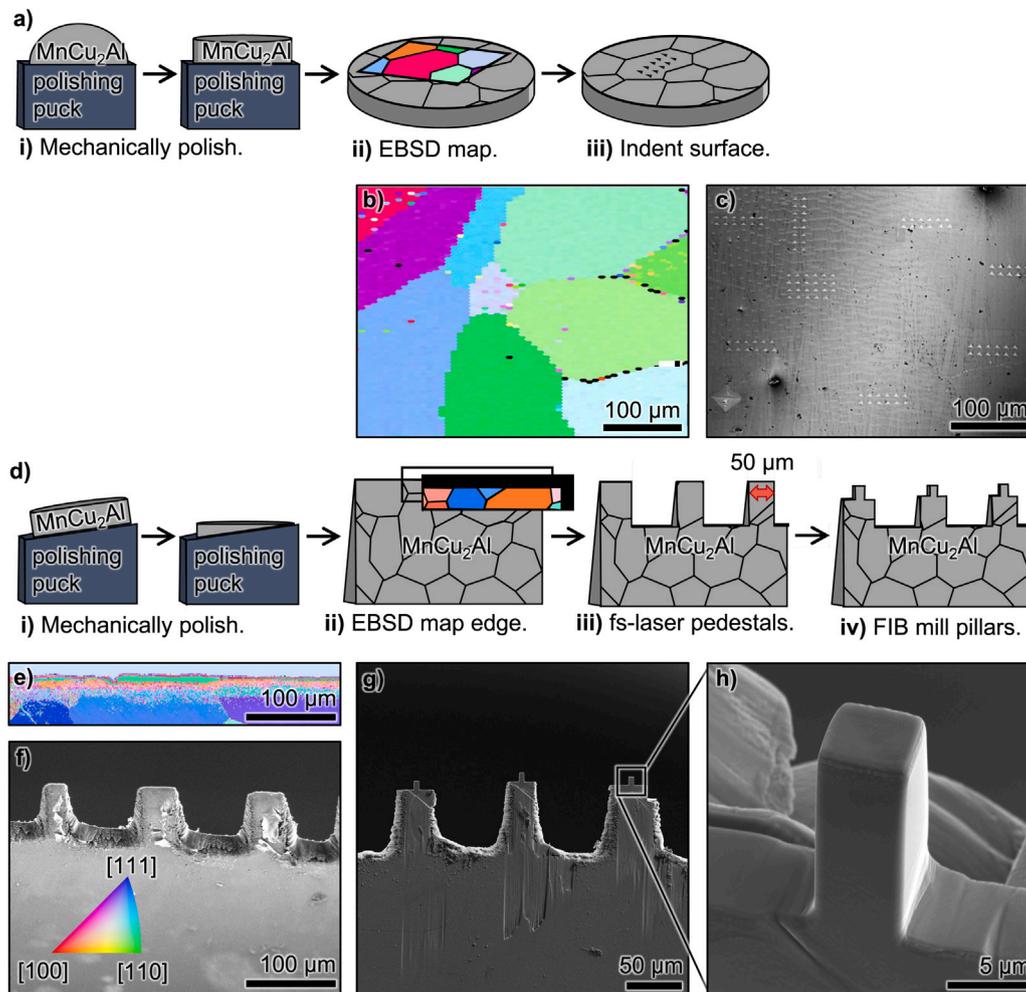
Fig. 1. (a) Schematic of the experimental workflow for orientation-specific nanoindentation. (b) An electron backscatter diffraction (EBSD) map of the region mapped for nanoindentation, corresponding to step a.ii. (c) A scanning electron microscope (SEM) image of the same region after indenting multiple grains. (d) Schematic of the experimental workflow used to prepare micro-pillars from a bulk polycrystalline sample. (e) An EBSD map of the wedge edge, corresponding to step d.ii. (f) SEM micrographs of pedestals machined from single-crystalline regions using a femtosecond laser with an approximate width of 50 μm, corresponding to step d.iii. (g) Micro-compression pillars milled from the top of each pedestal using a focused ion beam (FIB), within single-crystalline regions. (h) The resulting pillar geometry with a 5 μm × 5 μm cross-sectional area and gauge length of 10 μm. The total time necessary to complete this workflow totals approximately 85 h.

at 300 kV in bright field scanning transmission electron microscopy (BF STEM) mode and in TEM mode. Diffraction patterns collected in TEM mode were indexed using the JEMS diffraction pattern simulation package [49].

2.3. Mechanical testing

Mechanical test specimens for nanoindentation and micro-compression pillars were extracted from pieces of the bulk ingot of $MnCu_2Al$. Specifically, the nanoindentation test specimen was created from a tempered piece of the arc melted ingot that was mounted to an aluminum puck using crystal bond, ground using SiC paper, polished using diamond suspensions down to 1 μm, and vibratory polished using colloidal silica to a mirror finish (Fig. 1a.i.). While mounted to the aluminum puck, the polished surface was imaged using SEM and mapped using EBSD, to characterize the crystallographic orientation of visible grains (Fig. 1a.ii, b). Nanoindentation experiments were performed to test the mechanical properties of each grain orientation using a Nanomechanics iMicro Nanoindenter equipped with a 1000 mN load cell and Berkovich tip diamond indenter (Fig. 1a.iii, c). All nanoindentation data were collected using a continuous stiffness method operating at a frequency of 100 Hz, to a total depth of 1000 nm, and each data point reported in this investigation is representative

of at least 10–20 indents per crystallographic orientation, collected between depths of 400 nm–1000 nm [50]. Data recorded during the initial 400 nm of each indentation were excluded to account for surface roughness and possible surface artifacts introduced by polishing.

To create an accessible base for micro-pillar experiments, the polished specimen was remounted to an angled polishing puck and polished into a wedge-shaped geometry (Fig. 1d.i). Using EBSD mapping near the edge of the wedge-shaped specimen, several grains of interest were identified (Fig. 1d.ii, e), and were femtosecond laser machined *in situ* into single-crystalline pedestals using the TriBeam microscope, a laser-equipped TFS Versa 3D FIB-SEM (Fig. 1d.iii, Fig. 1) [51]. Micro-compression pillars were produced directly from the single-crystalline pedestals using the FIB to mill the pillar tops and sides perpendicular to the wedge surface with a slight taper, before removing all material from the faces to create pillars with a 1:1:2 aspect ratio to mitigate the potential impact of buckling (Fig. 1d.iv, g, h). A square pillar cross-section was employed to aid in the identification of active slip systems.

Micro-compression experiments were performed *in situ* in an TFS Apreo S SEM equipped with a Femto-tools FT-NMT04 Nanomechanical Testing System designed to optimize alignment during small-scale mechanical testing. Each pillar was loaded in a series of load *vs.* displacement tests until the point of yield using a displacement-controlled

method. After testing, the actuator displacement data were found to be linear with time for each loading step. Due to the additional compliance of the thin sample substrate and mounting, the measured displacement values are not only representative of the pillar, but also of the substrate and mounting setup. To determine displacements within the pillar alone, the length of the pillar was measured between the pillar's base and bottom of the Pt cap at the top of the pillar at stages throughout the loading sequence. The first SEM image corresponding to each loading sequence was taken as a reference for the displacement measurements collected at higher stresses and compared with SEM images up to the maximum displacement. The displacement *vs.* time data from the pillar measurements were fit using a linear regression and used to correct the raw displacement data. The compliance-corrected load vs. displacement curves were converted to stress vs. strain curves using the pillar dimensions.

A pillar with an [11 8 2] compression axis was selected to identify the active slip systems in MnCu$_2$Al. Slip trace analysis was performed on the pillar using a coordinate system described in the Supplemental Information to relate the EBSD orientation data with the slip traces identified on *post-mortem* images of the pillar as well as with features in the TEM images. The Schmid factors (*m*) for all potential slip systems for this pillar are presented in the Supplemental Information, along with the expected angle of incidence of each plane's slip trace with the pillar face.

Following SEM imaging, a detailed microstructural investigation was performed on an electron-transparent lamella micro-machined from the [11 8 2]-oriented pillar, using STEM imaging and a **g·b** analysis in the TEM. As the deformed material had high internal strains, the foil was prepared with three electron-transparent windows, framed by thicker regions for stabilization.

3. Modeling methods

To understand the structure and behavior of dislocations in this material, an *ab initio* informed PFDD method was employed. Originally developed for hcp, fcc and bcc metals [52–54], we describe how the PFDD framework is advanced here to treat faults and dislocations in the $L2_1$ crystal structure for the first time. The methods for these two components are described below.

3.1. Density functional theory calculations

All DFT calculations were performed within the Vienna *ab initio* simulation package (VASP) [55] using projector-augmented-wave (PAW) pseudo potentials [56,57] within the Perdew–Burke–Ernzerhof (PBE) generalized gradient approximation (GGA) [58] with a plane-wave energy cut-off of 500 eV. A Monkhorst–Pack scheme was used to construct the Brillouin zone [59] and spin polarization was also included. The magnetic moments of Mn, Cu and Al were initialized with values of 4 μ_B, 0.5 μ_B, and 0.5 μ_B, respectively.

γ-surface calculations were performed on supercells generated *via* the software package MultiShifter [60]. Specifically, the {110} γ-surface was sampled by a 15 × 21 grid along the [110] and [001] directions, respectively, with the total number of calculations then being further reduced by the mirror symmetries present within the $L2_1$ crystal structure. Periodic images of the planar faults were separated by greater than 16 Å and only structural relaxation normal to the plane of the fault was allowed. The computed energies are then used to fit a Fourier series with the form of

$$E^{\gamma}(\Delta_{001}, \Delta_{110}) = \Sigma_n \Sigma_m A_{nm} cos(\frac{2\pi n\Delta_{001}}{a_0} + \frac{2\pi m\Delta_{110}}{\sqrt{2}a_0}) \qquad (2)$$

where a_0 is the lattice parameter of MnCu$_2$Al determined from DFT, Δ_{001} is the shear displacement along the [001] direction and Δ_{110} is the shear displacement along the [110] direction, both relative to the unfaulted crystal.
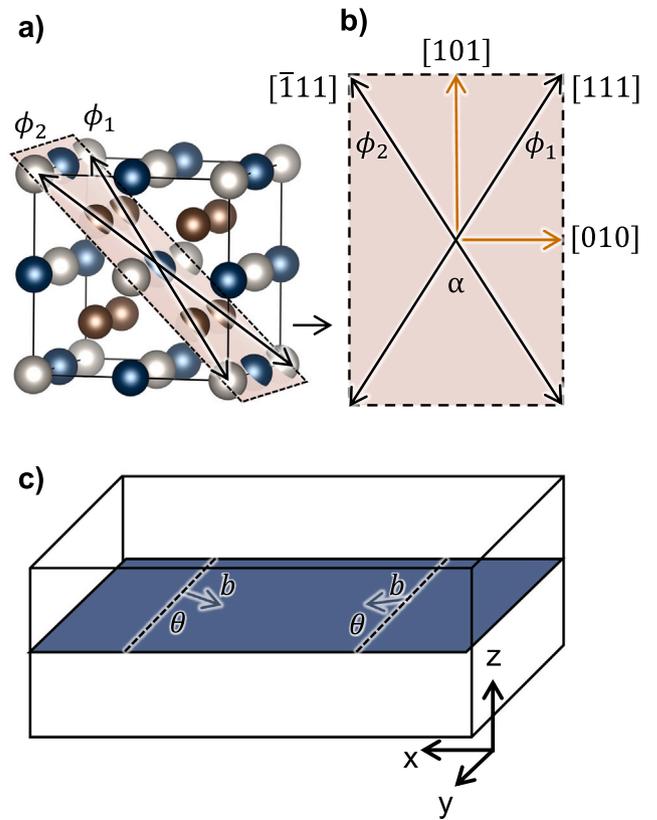
Fig. 2. (a) The Heusler intermetallic with the {110} slip plane highlighted. The two order parameters ϕ_1 and ϕ_2 lie along the two ⟨111⟩ directions within the {110} plane. (b) A schematic displaying the crystallography of the {110} plane. The two order parameters, which make an angle α with one another, are linearly independent and can therefore be used to describe any arbitrary displacement within the slip plane. This is used to parameterize the γ-surface in terms of the order parameters. (c) The simulation cell setup used for all phase field calculations reported within this study. The dislocation line is always oriented along the *y*-direction and the full Burgers vector is always $\vec{b} = \langle 111 \rangle$. In general, the Burgers vector can form an arbitrary angle θ with respect to the dislocation line. When $\theta = 0°$, a screw dislocation dipole is modeled, when $\theta = 90°$ an edge dislocation dipole is modeled.

3.2. Phase field dislocation dynamics simulations

In this section, we develop the PFDD formulation for the $L2_1$ Heusler system, building upon the theory that has been developed previously for the dynamics of dislocations across other crystal structures [53,54, 61–63].

Based on phase field theory, PFDD relies on order parameters, ϕ_i, that parameterize the extent of slip by dislocation(s) belonging to a specific slip system. The total energy of the system being studied, ψ, is then partitioned into three terms (i) the elastic energy, ψ_{elas} generated *via* the creation of a dislocation, (ii) the lattice energy, ψ_{latt}, which accounts for the nonlinear energy penalties associated with the large atomic displacements that will occur within the core of a dislocation, and (iii) the external energy, ψ_{ext}, which accounts for the work done *via* dislocation motion under an applied stress. Conventionally, the total energy density, ψ is then written as:

$$\psi = \psi_{elas} + \psi_{latt} - \psi_{ext} \qquad (3)$$

where the gradient term, which is known to capture the second-order effects of the core structure of fcc metals [52,63,64], has been omitted. A benefit of the phase field formalism is that it can be used to parameterize each of these energy terms into functions of the order parameter. Specifically,

$$\psi_{elas} = \int \frac{1}{2}[\epsilon(\boldsymbol{r}) - \epsilon^p(\boldsymbol{r})] \cdot \bar{\boldsymbol{C}} \cdot [\epsilon(\boldsymbol{r}) - \epsilon^p(\boldsymbol{r})]d^3r \qquad (4)$$

where $\epsilon(\mathbf{r})$ is the total strain within the system at point $\mathbf{r}$ and $\epsilon^p(\mathbf{r})$ is the plastic strain within the system at point $\mathbf{r}$ and $\bar{C}$ is the elastic stiffness tensor. The plastic strain can be expressed in terms of the order parameters:

$$\epsilon^p(\mathbf{r}) = \frac{1}{2} \Sigma_i \frac{b_i \phi_i(\mathbf{r})}{d_i} (\mathbf{s}^i \otimes \mathbf{n}^i + \mathbf{n}^i \otimes \mathbf{s}^i) \tag{5}$$

where $\mathbf{s}_i$ is the slip direction, $\mathbf{n}_i$ is the slip plane unit normal, b_i is the total Burgers vector associated with order parameter ϕ_i, and d_i is the interplanar spacing between two adjacent slip planes of order parameter ϕ_i within a given material system. $\otimes$ represents the dyadic product between two vectors. Additionally, the external energy, ψ_{ext}, is, in general, calculated as the following:

$$\psi_{ext} = \int \boldsymbol{\sigma}_{app} \cdot \epsilon^p(\mathbf{r}) d^3 r \tag{6}$$

In the case of the Heusler system, we focus on $\langle 111 \rangle \{110\}$-type dislocations. Therefore, within this contribution, $\mathbf{n}_i$ is a $\{110\}$ unit normal and slip is confined to the slip plane. As described above, and shown in Fig. 2b, there are two $\langle 111 \rangle$ slip directions within a $\{110\}$ plane that make an angle of $\cos(\alpha) = \frac{1}{3}$ with one another. i therefore ranges over the values $i = 1$ and $i = 2$. For a more detailed discussion on how the phase field model calculates the elastic energy based on anisotropic elasticity and the above expression for the plastic strain, please refer to [61].

Finally, the lattice energy is a material specific function that, for the Heusler intermetallic, has been formulated based on the γ-surface computed via DFT. Specifically, Eq. (2) is used to develop an expression for the γ-surface of the Heusler intermetallic:

$$\gamma_{gsfe}(\phi_1, \phi_2) = \frac{1}{2\sqrt{2}a_0^2} [E^\gamma(\phi_1, \phi_2) - E^\gamma(0,0)] \tag{7}$$

where the variables Δ_{001}, and Δ_{110} within Eq. (2) can be expressed in terms of the order parameters ϕ_1 and ϕ_2. Upon inspection of Fig. 2(b):

$$\Delta_{001} = a_0(\phi_1 - \phi_2) \tag{8}$$

$$\Delta_{110} = \sqrt{2}a_0(\phi_1 + \phi_2) \tag{9}$$

The expression for the lattice energy of the MnCu$_2$Al Heusler intermetallic, ψ_{latt}, then becomes:

$$\psi_{latt} = \int \frac{\gamma_{gsfe}(\phi_1(\mathbf{r}), \phi_2(\mathbf{r}))}{d} d^3 r \tag{10}$$

The total energy of the simulation cell is therefore a functional of the order parameters ϕ_1 and ϕ_2, and the system evolves by minimizing the total energy based on the time-dependent Ginzburg–Landau equation:

$$\frac{\partial \phi_i(\mathbf{r})}{\partial t} = -m_0 \frac{\delta \psi}{\delta \phi_i(\mathbf{r})} \tag{11}$$

m_0 is the relaxation coefficient and the time step is chosen to be smaller than the relaxation time, which is given by $1/\psi''m_0$, where ψ'' is the curvature in the free energy density. We find numerically that a time increment of $0.2/\mu$ – where μ is the effective isotropic elastic modulus – is sufficiently small to capture the relaxation processes and motion of interest here.

Simulations based on the theory described above are then carried out within a simulation cell that is discretized using a 3-dimensional grid containing 1024, 128, and 1024 grid points along the x, y, and z directions, respectively. Periodic boundary conditions are applied on all three directions. Initially, as shown in Fig. 2c, an undissociated perfect dislocation dipole, under zero applied stress, is inserted by assigning $\phi_1 = 1$, and $\phi_2 = 0$ to selected grid points. The left dislocation is located at $L_x/4$ from the left periodic boundary, and the right dislocation is located $L_x/4$ from the right periodic boundary of the simulation cell. The attraction between these two dislocations is cancelled out by the
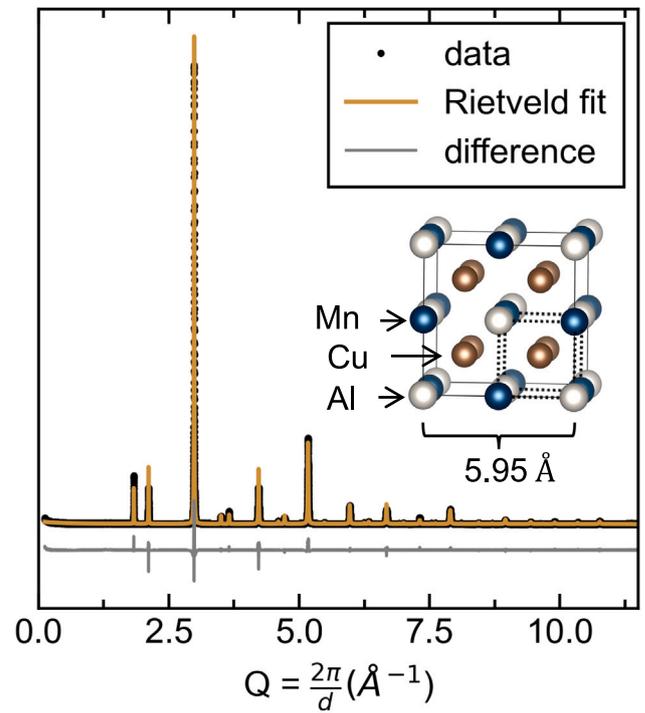
Fig. 3. Rietveld refinement of the MnCu$_2$Al synchrotron powder X-ray diffraction pattern demonstrates a well-ordered, single-phase Heusler ($L2_1$) microstructure with few crystallographic defects. MnCu$_2$Al in the $L2_1$ crystal structure (inset) indicates its relationship with the high-temperature $B2$ phase (dashed cell), upon disordering the Mn and Al atoms on their sublattices.

attraction between one of the dislocations and its neighboring dislocation within the adjacent periodic image, therefore ensuring that the dislocation dipole is in equilibrium. For edge and screw dislocations, respectively, in the Heusler system, the crystallographic orientations are $x[\bar{1}1\bar{1}] - y[\bar{2}\bar{1}1] - z[011]$ and $x[21\bar{1}] - y[\bar{1}1\bar{1}] - z[011]$. These initially undissociated dislocations then become extended by evolving the system via Eq. (11) until the Euclidean norm of the difference in global vector of each order parameter between successive iterations is smaller than 10^{-4}. The grid spacing along the x, y, and z directions is set to $b/4$ where $b = \sqrt{3}a_0$.

After studying the zero applied stress equilibrium configurations of both the edge and screw type $\langle 111 \rangle \{110\}$ dislocation dipoles, a pure shear stress is applied along the slip direction of the dislocation dipole and the response of the dipole is studied. Upon application of a critical shear stress, σ_p, the dipole begins to glide within the slip plane and the simulation is terminated when periodic images of the dipole annihilate with one another. This critical shear stress is then identified as the Peierls stress for each dislocation type. A more detailed discussion on the process employed to identify the Peierls stress is presented within [65].

4. Results

4.1. Determination of bulk phase ordering via X-ray diffraction

Given how the processing conditions influence phase ordering in MnCu$_2$Al, which could ultimately influence mechanical properties, we first assess the phases and crystalline quality of the measured samples. The phase purity of the tempered sample prepared in this investigation can be inferred from the synchrotron powder XRD data in Fig. 3. The Rietveld fit of the data to the $L2_1$ crystal structure accounts for each peak observed in the experimental data [66], and the lattice parameter associated with this fit ($a = 5.9533$ Å) is in good agreement with
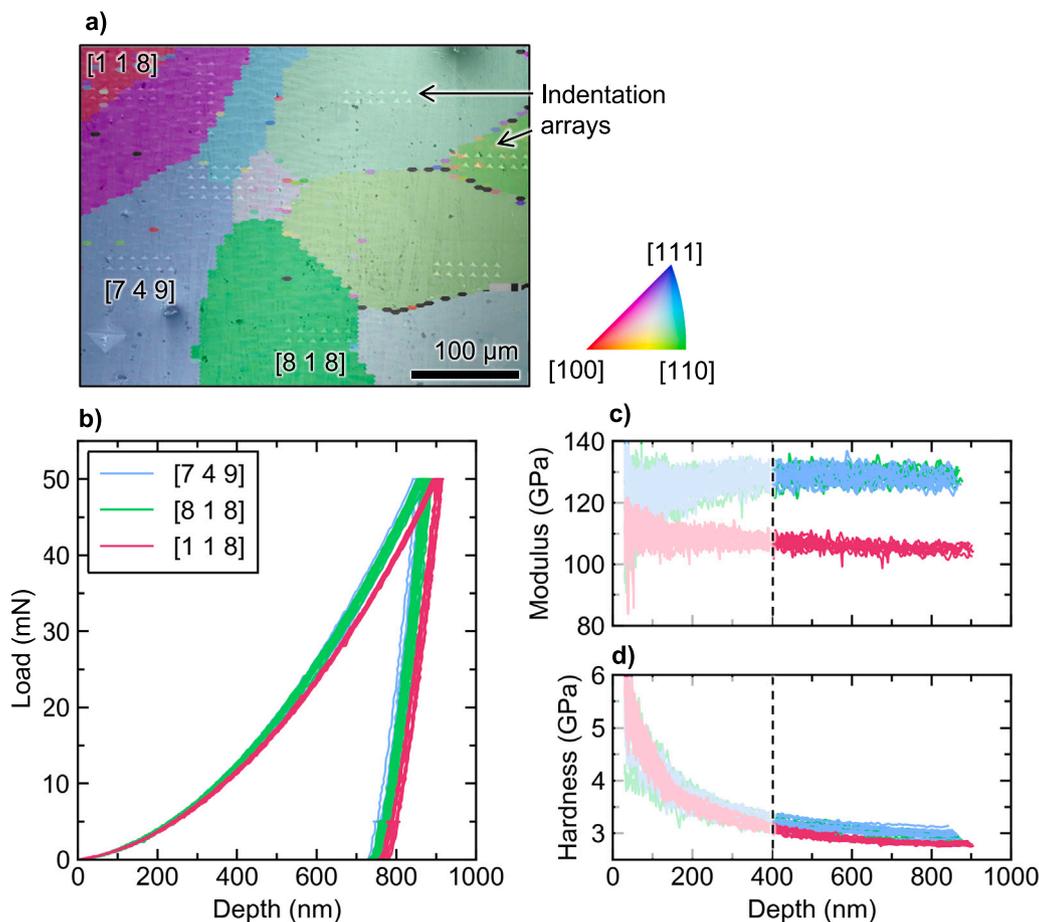
Fig. 4. (a) Electron backscatter diffraction map overlaid with scanning electron microscope image of nanoindentation arrays with the inverse pole figure (IPF) triangle to the right. (b) load *vs.* depth curves corresponding to indentation for selected orientations, colored using the IPF colors. (c–d) Modulus *vs.* depth and hardness *vs.* depth curves, indicating the spread in modulus and hardness with orientation from the approximate [100] minimum to approximate [111] maximum. Data recorded during the initial 400 nm of each indentation are excluded to eliminate the effects of surface roughness and artifacts formed during mechanical polishing to the intrinsic material properties. From all measured orientations, the average hardness was found to be 3.06 ± 0.35 GPa and the average modulus was 121.3 ± 7.6 GPa. (For interpretation of the references to color in this figure legend, the reader is referred to the web version of this article.)

previous reports of a = 5.934 Å [67] and a = 5.9615 Å [68], suggesting a single phase microstructure that has fully ordered in the $L2_1$ structure. Using the refinement to deconvolute the peak broadening effects of lattice strains from those of crystallite size, the lattice strains in the powder sample were found to decrease four-fold from ϵ = 0.0075 to ϵ = 0.0019 following the tempering step. This observation can be attributed to a reduction in $\langle 100 \rangle \{010\}$-type APBs [69] due to their annihilation during the tempering step [39–41], which mitigates the potential effects of pre-existing defects on the measured mechanical properties of samples.

4.2. Elucidation of strength and compressive plasticity in MnCu$_2$Al using micro-mechanical testing

We next focus our attention to measurements of single crystalline mechanical behavior measured using small-scale testing. Nanoindentation experiments using a continuous stiffness method were first performed to provide a rapid assessment of the bulk hardness and modulus. Fig. 4 highlights grains of several orientations, overlaid with an SEM image of the indentation arrays. The load *vs.* depth, modulus *vs.* depth, and hardness *vs.* depth curves corresponding to the [7 4 9], [8 1 8], and [1 1 8] out-of-plane orientations are plotted in Fig. 4b–d. These orientations are near the [1 1 1], [1 0 1], and [0 0 1] orientations, respectively, giving a representation of possible anisotropy in the modulus (E_{hkl}) and hardness (H). In our measurements, and in general, the elastic anisotropy ratios detected through Berkovich indentation are lower

than expected through uniaxial compression due to the multi-axial nature of indentation relative to uniaxial compression [70]. Nevertheless, the method has been shown to be sensitive to orientational trends in elastic modulus that result from elastic anisotropies [70–72], as observed in Fig. 4c.

Across all orientations, the average hardness was 3.06 ± 0.35 GPa, with only slight orientation-dependent deviations. In contrast, the average modulus was 121.3 ± 7.6 GPa, but had a discernible orientation-dependent trend in the modulus, with low modulus in the [0 0 1] direction, and increasing modulus as the angle between the load and [0 0 1] is increased. Anisotropy in the measured modulus can be observed in the modulus *vs.* depth data plotted in Fig. 4c, between the [7 4 9] and [8 1 8] orientations, which have a higher value than the [1 1 8] orientation, which is closest to the [0 0 1] axis. Anisotropy in the modulus is further discussed in the Supplemental Information.

Using single crystalline micro-mechanical specimens, we next measure the MnCu$_2$Al full mechanical response in uniaxial compression, as a function of orientation. Stress *vs.* strain curves corresponding to the micro-compression experiments are plotted in Fig. 5. Loading was performed in increments to determine the onset of plastic deformation and to enable detailed slip trace identification prior to failure. Signatures of plastic deformation are evident in the stress–strain curves of all pillars. In some cases, the onset of yielding is characterized by a deviation from the linear elastic loading curve, followed by a quasi-continuous strain hardening response (e.g. [11 8 2] compression axis pillar). In other cases, measurable load drops can be detected near the
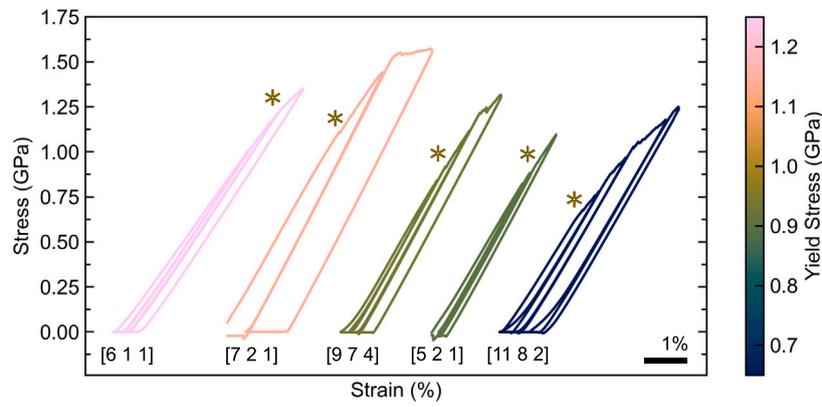
Fig. 5. Stress *vs.* strain curves acquired during the compression of micro-pillars across a spread in orientations demonstrates a strong relationship between pillar orientation and yield stress, indicated at the onset of plasticity with a star. The average yield stress was found to be 0.90 GPa ± 0.18 GPa. Note that the pillars were loaded and unloaded multiple times and were not deformed to the point of failure.
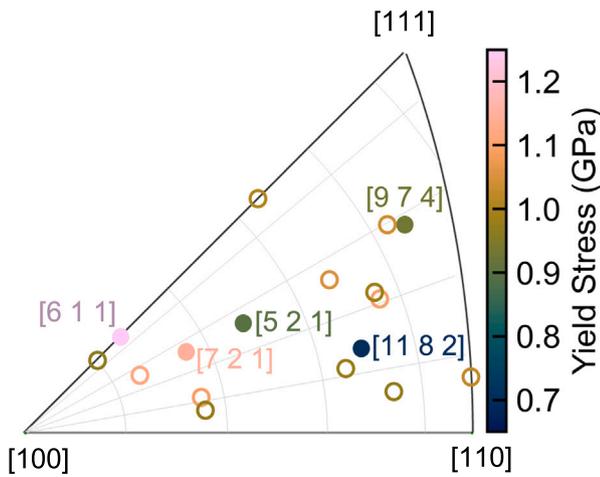
Fig. 6. Orientations of pillars are displayed as the filled points on the inverse pole figure map, with coloring by yield stress. Hollow points on the map correspond to nano-hardness data (H) converted to yield stresses using the standard Tabor relationship (Eq. (12)) [73]. The results show that yield stress is correlated to orientation. (For interpretation of the references to color in this figure legend, the reader is referred to the web version of this article.)

Table 1
Schmid factors (m) calculated for $\langle 111 \rangle \{110\}$, $\langle 111 \rangle \{112\}$, and $\langle 111 \rangle \{123\}$ slip families in a [11 8 2]-oriented pillar. The three highest Schmid factors are bolded.

	Slip direction $[uvw]$	Slip plane (hkl)	Schmid factor m	Angle θ
1	$[11\bar{1}]$	(011)	0.367	18.9°
2	$[11\bar{1}]$	(101)	**0.477**	45.0°
3	$[111]$	$(10\bar{1})$	0.408	3.8°
4	$[11\bar{1}]$	(112)	**0.488**	22.6°
5	$[11\bar{1}]$	(211)	0.339	61.5°
6	$[111]$	$(11\bar{2})$	0.393	49.6°
7	$[111]$	$(\bar{2}11)$	0.314	127.2°
8	$[11\bar{1}]$	(123)	**0.499**	10.5°
9	$[11\bar{1}]$	(213)	0.458	32.1°
10	$[11\bar{1}]$	$(\bar{1}32)$	0.402	53.9°
11	$[1\bar{1}1]$	$(12\bar{3})$	0.411	58.8°
12	$[111]$	$(13\bar{2})$	0.360	100.1°
13	$[111]$	$(21\bar{3})$	0.360	37.2°

point of yielding (e.g. [7 2 1] compression axis pillar). We assign a yield stress as the point of clear deviation from linear fits to the loading curves. Depending on compression axis orientation of the pillar, yield stresses range between $\sigma_Y = 1.25$ GPa and $\sigma_Y = 0.65$ GPa, as marked by stars in Fig. 5. Regardless of orientation, plastic flow was clearly observed, though the apparent strain hardening rate appeared to be inversely related to yield stress. In the case of the [7 2 1] pillar, a 2nd stage of plasticity is evident as a regime with nearly constant flow stress following an initial hardening regime. While such behavior was not measured in other pillars, this is likely since the tests were interrupted while still in the initial stages of strain hardening. In general, pillars oriented close to [1 0 0] had high yield stresses, but reduced hardening, while pillars closer to [1 1 0] or [1 1 1] had low yield stresses, yet large capacities for hardening. No large scale shear bands or cracks were detected in any of the pillars compressed *in situ* in the SEM. Taken as a whole, MnCu$_2$Al demonstrates measurable and stable plasticity when undergoing micro-pillar compression *in lieu* of catastrophic shear localization or fracture.

We next compare the orientation-dependence of yield stresses measured by micro-pillar compression and hardness measured by nanoindentation, using the standard Tabor relationship,

$$\sigma_Y = \frac{H}{3} \tag{12}$$

[73], which are shown together as a function of crystal orientation in Fig. 6. The estimated average yield stress from nanoindentation is 1.02 ± 0.35 GPa, while the average yield stress of the micro-pillar experiments was 0.90 GPa ± 0.18 GPa, with the possible differences arising from differences in the crystal orientations sampled or the presence of substantial strain hardening beyond the onset of yield. In both sets of data, there are notable trends of yield stress with orientation, though they are more prominent in the micro-pillar experiments. This discrepancy may be due to the multi-axial nature of indentation experiments, which inherently probes multiple slip modes due to the stress states induced by the indenter tip, thereby self-averaging any potential plastic anisotropies [70]. In general, it can be observed that yield stress decreases progressively with changes in orientation from the [100] axis, where it is at its maximum, as the angle between the load and [100] is increased.

4.3. Characterization of {110}-type slip using slip trace analysis

The [11 8 2]-oriented pillar, which displayed a high rate of strain hardening after yielding, was selected to further characterize the slip modes and defect structures activated in the MnCu$_2$Al structure. Schmid factors, m, were calculated for each of the 12 {110}-type, 12 {112}-type, and 24 {123}-type slip modes (see Supplemental Information), to determine the planes experiencing the highest resolved stresses within the [11 8 2]-oriented micro-pillar. Slip modes that had a Schmid factor greater than m = 0.3 are tabulated in Table 1. The highest Schmid factors within each slip family are bolded to indicate which systems are expected to be active, and were $m_{(123)} = 0.499$, $m_{(112)} = 0.487$,
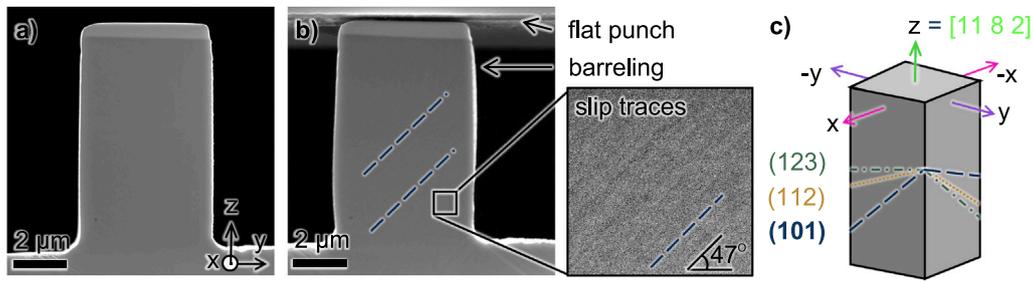
Fig. 7. Scanning electron microscope (SEM) micrographs of the [11 8 2]-oriented micro-pillar (a) before and (b) after compression. Plastic deformation is evidenced by barreling and the appearance of (101) slip traces inclined from the image top right to the bottom image left at an angle of $\theta = 47°$. (c) Schematic depiction of the coordinate axes used to index slip traces, marked with the expected slip traces of the (123), (112), and (101) slip planes.

Table 2

Expected contrast evaluation for the $\langle 111 \rangle$ slip direction family considering the $\mathbf{g} \cdot \mathbf{b}$ effective invisibility criteria using the $\mathbf{g}_{02\bar{2}}$ and $\mathbf{g}_{20\bar{2}}$ diffraction conditions. Conditions with $\mathbf{g} \cdot \mathbf{b} = 0$ are expected to be invisible, while all other conditions are expected to be visible.

Slip direction	$\mathbf{g}_{02\bar{2}}$	$\mathbf{g}_{20\bar{2}}$
Observed	Visible	Invisible
[111]	Invisible	Invisible
[$\bar{1}$11]	Invisible	Visible
[1$\bar{1}$1]	Visible	Invisible
[11$\bar{1}$]	Visible	Visible

and $m_{(101)} = 0.477$, corresponding to the [11$\bar{1}$](123), [11$\bar{1}$](112), and [11$\bar{1}$](101) slip modes, respectively. Based on this assessment, and the assumption that all slip families are potentially active, we would expect to see preferential activation of the (123) slip plane for this compression axis.

To experimentally determine the active slip mode, the [11 8 2]-oriented pillar was imaged following deformation, revealing the appearance of diffuse slip traces at $\theta = 47°$ from the pillar base (Fig. 7a–b). Out of all the possible 12 {110}-type, 12 {112}-type, and 24 {123}-type slip modes, the (101) plane was found to be the closest match to the experimental trace, with a misorientation well below the 5° misorientation threshold that can be attributed to experimental error (2°) [74]. Slip traces for each of the highest Schmid factor slip planes are superimposed on the faces of the schematic pillar in Fig. 7c for comparison with the measured trace. Slip traces on the other pillars are consistent with the activity of a single family of slip traces on the {110} plane, even when the maximum resolved shear stress plane was expected to be of composite slip. These observations suggest that the {110} slip family governs deformation in MnCu$_2$Al at ambient temperatures, even in pillars oriented for net slip on a maximum resolved shear stress plane.

4.4. Characterization of slip direction from post-mortem TEM $\mathbf{g} \cdot \mathbf{b}$ analysis

Experimental determination of the slip direction was performed *via* the effective invisibility criteria $\mathbf{g} \cdot \mathbf{b} = 0$ using conventional TEM on a lamella extracted from the [11 8 2]-oriented micro-pillar following deformation to 4.2% total strain. Here, $\mathbf{g}$ is the reciprocal lattice vector used within a two beam condition to form the TEM image, $\mathbf{b}$ is the Burgers vector of the dislocation, and the $\mathbf{g} \cdot \mathbf{b} = 0$ condition is the invisibility criterion used to determine the displacement vector of crystal dislocations. The micrographs in Fig. 8b–d were collected from the region of the foil indicated by the black square in Fig. 8a, which was located near a heavily deformed region and presumably within one of the slip bands. For the $\mathbf{g}$-vector of (02$\bar{2}$), all dislocations remain visible (Fig. 8c), whereas all dislocations become invisible using the (20$\bar{2}$) two-beam condition (Fig. 8d), suggesting a common Burgers vector for the dislocations within the field of view. Generally, at least two cases of invisibility are desirable to unequivocally define a Burgers

vector. Nevertheless, the data in Table 2 from the [11 8 2]-oriented micro-pillar is consistent with dislocations with a Burgers vector of $\mathbf{b}$ = [11$\bar{1}$]—the slip direction of the [11$\bar{1}$](101) slip mode, the highest Schmid factor within the {110} slip family for this pillar orientation.

We also considered the presence or absence of partial dislocations and the planar faults between them. In cases where fractional slip leads to planar faults, the presence of partial dislocations in the slipped region could be detected when there is evidence for pairs or multiples of dislocations traveling together [37,42]. In the *post-mortem* images in Fig. 8, the spacing between all defects appears to be roughly consistent, with no clear spatial pairing of partial dislocations. A more direct method is to directly image planar faults that could arise from slip by partial dislocations. Depending on the particular partial Burgers vectors involved in the dissociation mechanism, the resulting planar defect may form an antiphase boundary, which produces what is often referred to as 'antiphase contrast' under the proper TEM imaging conditions [18, 42]. If some of the dislocations in Fig. 8 are actually partial dislocations, bounding an antiphase boundary, we may expect to observe antiphase contrast when imaging using the $\mathbf{g}$ = (220), (200), or (111) superlattice reflections [42]. The images in Fig. 8c–d are imaged using the $\mathbf{g}_{\{220\}}$-type superlattice reflections, yet no antiphase contrast is discernible in the images.

The absence of antiphase contrast, even in the possible presence of antiphase boundaries, can be explained by the results of Venkateswaran et al., who calculate the orientation-dependent extinction distances, ξ_g, necessary for producing antiphase contrast in the MnCu$_2$Al Heusler [42]. They reported ξ_g for the (220), (200), and (111) superlattice reflections, to be $\xi_{(220)} = 38$ nm, $\xi_{(200)} = 1107$ nm, and $\xi_{(111)} = 332$ nm. Considering the criterion of $\xi_g \leq 2t$, where t is the foil thickness, for distinct antiphase contrast and our average TEM foil thickness of approximately 100 nm, antiphase contrast may be only partially visible in the $\mathbf{g}$ = (220) imaging condition. This implies that even if there are antiphase boundaries present in MnCu$_2$Al following plastic deformation, the absence of antiphase contrast does not definitively negate their presence, even in our micrographs using the (220)-type imaging conditions in Fig. 8c–d. We note that to best understand and characterize complex core dissociations – which have also been observed in hexagonal close-packed materials, intermetallic compounds, and oxides [20,75] – a combination of high-resolution TEM experiments and simulated TEM micrographs are more suitable than conventional imaging with diffraction contrast. However, three possible scenarios (or some combination thereof) are consistent with the imaging we have performed: the defects in the image are either 1. non-dissociated dislocations with the $\langle 111 \rangle$ slip direction, 2. all partial dislocations of the slip direction $\langle 111 \rangle$ without the characteristic antiphase contrast (due to the large extinction distances), or 3. $\langle 111 \rangle$ dislocations that involve dissociation events that lead to splitting widths below the resolution of our micrographs.
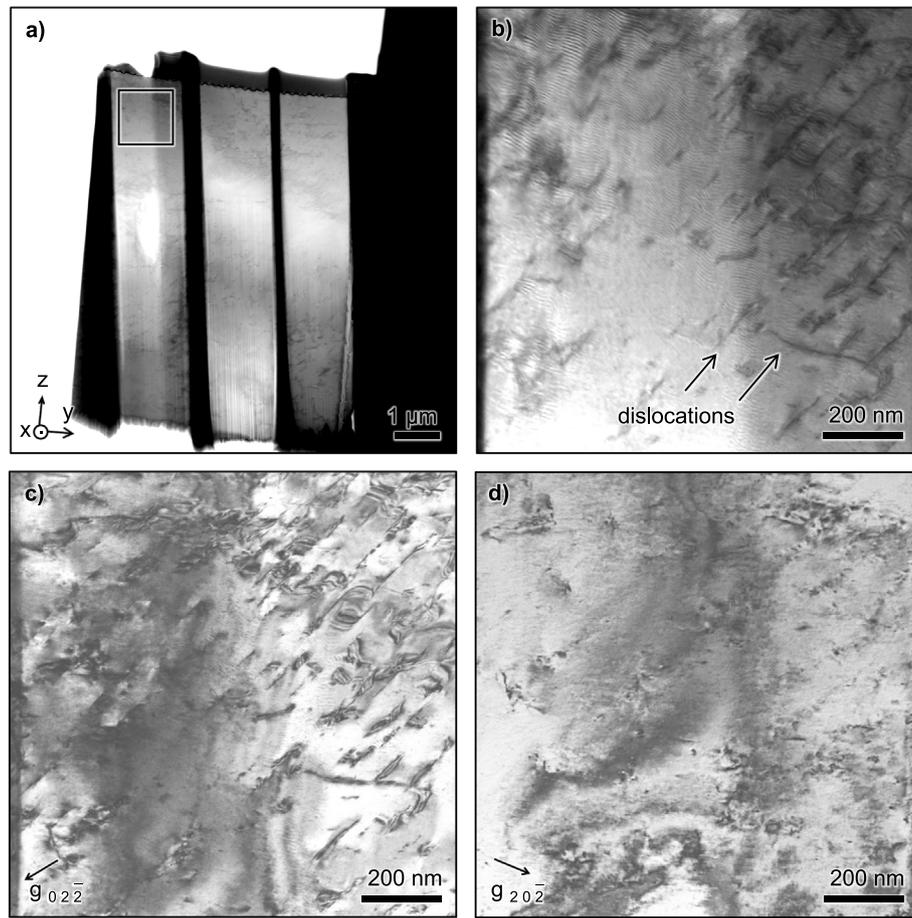
Fig. 8. (a) A bright field scanning transmission electron microscope (BF STEM) micrograph of a lamella pulled from the deformed [11 8 2]-oriented micro-pillar, with three electron-transparent windows to provide support to the strained microstructure. (b) A BF STEM micrograph collected from the region indicated in (a) reveals dislocations with a major texture inclined in the same direction as the slip traces in Fig. 7b. (c–d) Transmission electron micrographs in the $\mathbf{g}_{02\bar{2}}$ and $\mathbf{g}_{20\bar{2}}$ diffraction conditions demonstrate the visibility and invisibility criteria, respectively. Table 2 gives the evaluation of the possible $\langle 111 \rangle$-type defects in comparison with the observed visibility and invisibility criteria.

5. Discussion

Our experimental investigation of the Heusler intermetallic in single crystalline form at room temperature reveals clear evidence of stable and consistent plastic deformation, with no evidence for significant shear localization or cracking, despite prior reports of brittle behavior at low temperatures [36,38]. It is worth noting that our loading experiments were terminated before failure, so the complete ductility of $MnCu_2Al$ was not fully explored in this study. Nevertheless, previous observations have shown that $MnCu_2Al$ can deform to more than 20% shear stress [36]. The extent of plasticity, strength, and ductility in bcc-based materials is generally influenced by the characteristics of the defect structures that mediate plasticity [20,76]. In our *post-mortem* electron microscopy examination, we considered the presence of partial dislocations and planar faults, but were unable to conclusively determine whether the defect structures present could be characterized as either undissociated dislocations, antiphase boundaries, or stacking faults. The lack of a clear understanding of the elementary characteristics of the defects in $MnCu_2Al$ hinders our ability to ascertain the mechanisms responsible for the degree of unexpected strength and plasticity observed in our compression experiments, and their relationship to properties observed in other bcc-derived intermetallics. To address this challenge, we assess the intrinsic capacity for plastic deformation in $MnCu_2Al$ using published elastic constants and their anisotropies. Furthermore, we combine DFT and phase field simulations to investigate the core structure of $MnCu_2Al$ $\langle 111 \rangle \{110\}$ dislocations and their critical stresses and then compare the result to our measurements.

Table 3
$MnCu_2Al$ elastic constants, C_{ij}, Zener anisotropy ratio, A^*, sourced from the literature.

C_{11} (GPa)	C_{12} (GPa)	C_{44} (GPa)	A^*	Source
Experimental				
137.0	80.5	99.6	3.53	[37]
135.3	97.3	94	4.95	[68]
DFT				
138.8	113.9	102.9	8.27	[77–79]
143.7	116.1	117.6	8.52	[67]
138.0	117.0	103.0	9.81	[80]
137.0	115.0	112.0	10.18	[81]
170.13	145.17	129.76	10.40	[82]
137.2	117.8	105.3	10.83	[82]

5.1. Capacity for plastic deformation in Heuslers

We construct Blackman [83] and Every [84] diagrams to visualize the relationship between the $MnCu_2Al$ elastic constants and intrinsic ductility and crystal structure stability, respectively. These tools have been employed to investigate the elastic properties of cubic crystals [85, 86] and have previously been applied to the Heusler material system by Wu et al. [67]. In the Blackman diagram in Fig. 9a, values falling along the zero Cauchy pressure line, $p_C = C_{12} - C_{44} = 0$ are considered ideal Cauchy solids. The Zener anisotropy ratio that quantifies anisotropy in
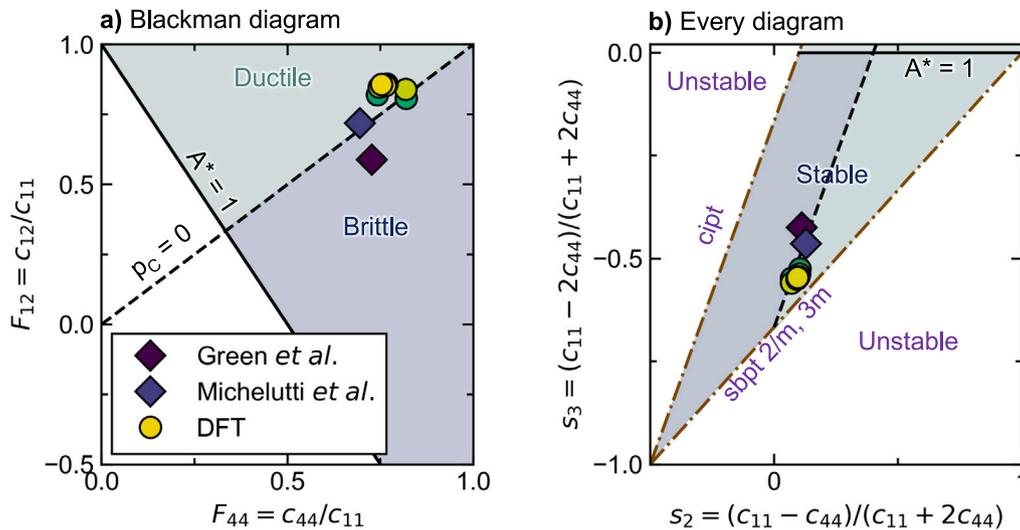
Fig. 9. (a) Blackman and (b) Every diagrams. In both diagrams, the black line indicates isotropy ($A^* = 1$) and the black dashed line indicates the ideal Cauchy pressure ($p_C = 0$). In the Every diagram, the Born criteria define a phase stability triangle marked by the brown dash-dotted lines. Cubic isomorphic phase transitions (cipt) and symmetry breaking phase transitions (sbpt) occur upon transgressing the dash-dotted lines into an elastically unstable regime.

cubic materials,

$$A^* = \frac{2C_{44}}{C_{11} - C_{12}} \tag{13}$$

($A^* = 1$ is the isotropic case) can also have implications for elastic instability [67], defect stacking fault width [61,87,88], and the dominance of edge $vs.$ screw dislocations [75]. All A^* calculated for MnCu$_2$Al (Table 3) are large, positive values—positioning them in the top right corner of the diagram, with the computational results clustered toward the extreme. According to Pettifor's criteria for ductility in intermetallics, materials with $p_C > 0$ are considered ductile, while materials with $p_C < 0$ are considered brittle [89]. As all points for MnCu$_2$Al are grouped around the Cauchy line, this suggests that MnCu$_2$Al is on the cusp of the brittle/ductile distinction—with some capacity for plastic deformation, yet maintaining a covalent bonding scheme.

In the Every diagram, visualization of elastic anisotropy and Cauchy pressure is combined with a metric for crystal stability (Fig. 9b). Parameters based on the cubic elastic constants, $s_3 = (C_{11} - C_{12} - 2C_{44})/(C_{11} + 2C_{44})$ and $s_2 = (C_{11} - C_{44})/(C_{11} + 2C_{44})$, are compared in order to distinguish the severity, and nature, of the elastic instabilities of the material (cubic isomorphous $vs.$ symmetry breaking phase transitions) [67,85]. According to Born's shear criterion, values falling outside the stability triangle denominated by the dash-dotted cubic isomorphic phase transition (cipt), symmetry breaking phase transition (sbpt), and solid isotropic case represent unstable crystal systems [67,84]. As in the Blackman diagram, all values reported in Table 3 are grouped about the dashed Cauchy line. It is apparent that the high-anisotropy computational reports predict a material on the verge of a symmetry-breaking phase transition, which is not consistent with the experimental reports of the Heusler phase stability or of the experimental elastic constants. Clearly further studies are required to determine the reason for this discrepancy between the computational and experimental elastic constants. Based on this analysis, it appears that the experimental elastic constants presented either by Michelutti et al. or Green et al. [36,68] correctly capture the phase stability and ductility of MnCu$_2$Al.

5.2. Linking defect structure and plasticity in bcc-derived materials

The observed $\langle 111 \rangle \{110\}$ slip mode that we measure experimentally is reminiscent of other bcc-based alloys and intermetallics. We elaborate on this commonality here since the $Fm\bar{3}m$ space group of the

$L2_1$ crystal structure may, at first, conceal the fact that the Heusler intermetallic is in fact bcc-derived (with the resemblance depicted in the Heusler unit cell in Fig. 3) [25,37,38,40]. The diffraction peaks in the structure's XRD spectrum reflect the presence of an underlying bcc lattice, as the (111) peak that is uniquely attributed to the $L2_1$ structure, is succeeded first by the (200) peak, then by the (220) peak—signatures of the $B2$ and $A2$ (bcc) motifs within the $L2_1$ structure. While the collective results suggest that the $L2_1$ structure behaves mechanically as a bcc-derived structure, rather than an fcc-derived structure, the nature of potential dislocation dissociation reactions, and the resulting planar faults caused by plastic deformation, are not clear.

Investigations of bcc-derived materials have demonstrated that their deformation is often characterized by non-planar screw dislocation cores, which severely restrict dislocation glide and often leads to brittle mechanical behavior at temperatures below the ductile to brittle transition [76]. The best known example of this is in bcc metals, wherein the cores of $\frac{1}{2}\langle 111 \rangle$ screw, spread onto three intersecting $\{110\}$ planes, whereas edge dislocations are planar. Consequently, screw dislocations must overcome a high Peierls barrier to glide, whereas edge dislocations glide with much greater ease [43,76,90].

In our micro-pillar loading experiments, the sample is expected to begin with a low density of dislocations. Thus, the onset of yield is likely associated with the Peierls stress required to move existing dislocations in the single crystal that are not blocked by any preexisting obstacles. The presence of non-planar dislocation cores in MnCu$_2$Al would then likely lead to a high yield stress (Fig. 5), a limited capacity for plasticity, and the presence of long straight screw dislocations following deformation [43]. In contrast, dislocations that can dissociate into partials to form stacking faults or antiphase boundaries, generally remain planar and are more glissile than their non-planar counterparts [20]. This explanation is more consistent with the behavior observed in the loading curves, which demonstrated high yield stresses, followed by a high capacity for stable plastic flow and strain hardening. We explore this hypothesis with additional computational techniques, which include predicting the defect structure of $\langle 111 \rangle \{110\}$ dislocations within MnCu$_2$Al, to rationalize the observed mechanical properties.

5.3. γ-surface calculations of the $\{110\}$ slip plane in MnCu$_2$Al

We calculate the $\{110\}$ γ-surface to aid in the prediction of planar defect structures. In Fig. 10a, the MnCu$_2$Al $\{110\}$ slip plane is indicated
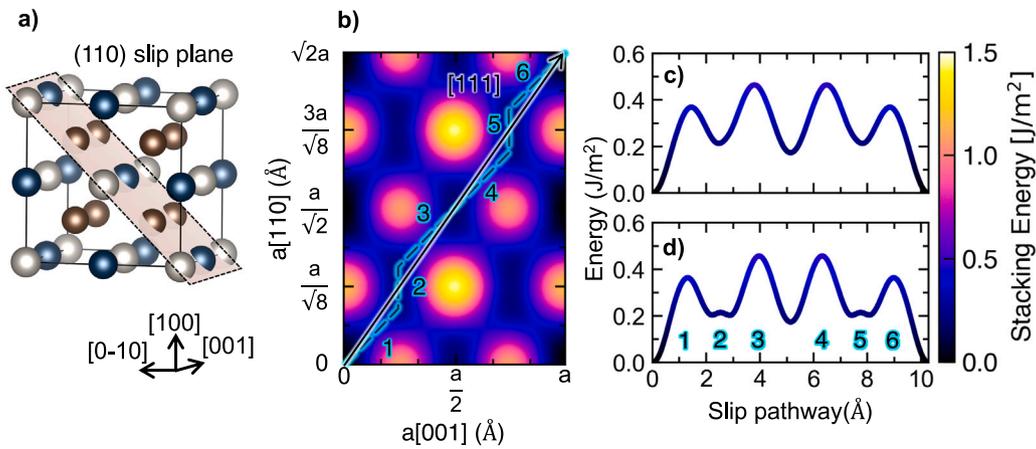
Fig. 10. (a) Heusler structure, indicating its relationship to the (110) slip plane. (b) Interfacial stacking energies for (110)-type planar faults in MnCu$_2$Al, as a function of the displacement vector. The [111] slip vector is overlaid in white, while a modified slip path suggested by the position of stacking energy minima is overlaid dashed in cyan. Stacking energy (J/m^2) *vs.* net slip in the [111] direction (Å) for (c) the [111] slip pathway marked by the solid line in (b) and (d) the modified [111] slip pathway, plotted in the dashed line in (b). (For interpretation of the references to color in this figure legend, the reader is referred to the web version of this article.)

in relation to the unit cell, while the corresponding calculated γ-surface along slip coordinates normalized by the MnCu$_2$Al lattice parameter, *a*, is displayed in Fig. 10b. γ-surfaces are commonly used for qualitatively predicting potential slip directions and dissociation mechanisms, as well as for identifying materials that are likely to host planar dislocation cores. It is often the case that a material system with a γ-surface that contains local minima will dissociate into planar partials, forming stacking faults, rather than into non-planar core configurations that tend to be less glissile [20,76,91]. Since the {110} γ-surface of MnCu$_2$Al has a number of local minima, the dissociation of dislocations within MnCu$_2$Al into planar partials is to be expected.

Inspection of the γ-surface demonstrates the $\langle 111 \rangle$ slip pathway as a potential low-energy slip pathway, with four local minima in the stacking energy, positioned at the $\frac{1}{4}[111]$ sites (Fig. 10b–c). A dislocation dissociation mechanism based on this pathway is consistent with the dissociation mechanism in Eq. (1). However, further analysis of the relative minima positioned near the [111] slip direction suggest an alternative slip path (dashed cyan line in 10b and profile in 10d). The plot of stacking energy along this pathway shows that there are six local minima in the stacking energy and a net reduction in the stacking energy. The modified slip pathway is described by the dissociation mechanism in

$$[111] = b_1 + b_2 + b_1 + b_1 + b_2 + b_1, \tag{14}$$

where $b_1 = \frac{1}{4}[\alpha, \alpha, 1]$ and $b_2 = \frac{1}{2}(1 - \alpha)[1, 1, 0]$. In MnCu$_2$Al, $\alpha \approx \frac{3}{4}$. The approximate products of this mechanism have been previously observed in the context of the related *B*2 intermetallics [20] with a reaction following the general form of

$$[111] = b_1 + b_2 + b_1, \tag{15}$$

where the slip vectors, $b_1 = \frac{1}{4}[\alpha, \alpha, 1]$ and $b_2 = \frac{1}{2}(1 - \alpha)[1, 1, 0]$. Lin et al. found that the value of α depended strongly on the chemistry of the bcc-derived *B*2 intermetallic [20]. While the modified slip pathway in MnCu$_2$Al has a net increase in length, the peak energy barrier that needs to be overcome to reach the second minima *via* b_2 is significantly smaller than that of the peak energy barrier necessary to reach the $\frac{1}{2}\langle 111 \rangle$ position, which may influence the preferred slip pathway to be more similar to that of *B*2 intermetallics. Both dissociation reactions vectorially sum along $\langle 111 \rangle$, in alignment with the experimentally-observed net Burgers vector, $\vec{b} = \langle 111 \rangle$.

While predictive, the γ-surface alone, only provides stacking fault energies and cannot quantitatively predict the stacking fault width that would separate partials that participate in a hypothesized dissociation reaction, let alone the resolved shear stress required to move the

equilibrated dislocation core. One potential approach to ascertain the stacking fault width is to treat each partial dislocation as a singular Volterra dislocation [20]. However, this method requires fixing the partial dissociation reaction, which limits its ability to differentiate between different dissociation reactions and allow partial dislocation cores to spread. The PFDD model was, therefore, developed for the Heusler intermetallic in order to predict the energetically favorable dissociation reaction, the core structure, and fault width. It is also employed to estimate the critical stress to move the resulting defects, which can be directly compared to our experimental measurements.

5.4. Modeling Heusler defect structures with phase field dislocation dynamics simulations

Using PFDD, we first allow an initially compact, $\langle 111 \rangle\{110\}$ dislocation, under zero applied stress, to relax to its energetic minimum *via* the minimization of the system's competing elastic and lattice energies. The energy minimum realized by the edge type dislocation, under zero applied stress, is shown in Fig. 11a. The final configuration realized by this dislocation involves significant spreading within its {110} slip plane. The values of the in-plane disregistry along the $\langle 211 \rangle$ crystallographic direction are reflected in the coloring of Fig. 11a to best highlight the complex dissociation reaction that is expected for MnCu$_2$Al. For an edge dislocation, the disregistry in the $\langle 211 \rangle$ direction represents the slip normal to the $\langle 111 \rangle$ direction. For reference, an edge dislocation that has not undergone a dissociation event would present itself as a thin white strip with a single dashed fault line, separating the unslipped (left) and slipped (right) region of the material. Instead, we observe spreading on the {110} slip plane with significant disregistry orthogonal to the initial $\langle 111 \rangle$ slip direction. Each large jump in the $\langle 111 \rangle$ and $\langle 211 \rangle$ disregistry is interpreted as a partial dislocation, leading to the identification of six partials upon dissociation. The total splitting width of the fault is 24 nm, or 23.5*b*, in units of the $\langle 111 \rangle$ Burgers vector. Since the splitting is greater than *b*, the defect is regarded as dissociated [20].

The disregistry within the faulted region of Fig. 11a, projected along the $\langle 111 \rangle$ and $\langle 211 \rangle$ crystallographic directions, are plotted in Fig. 11b. Plateaus in the $\langle 111 \rangle$ trace indicate regions that are reminiscent of a stacking fault, and/or antiphase boundary. For the edge dislocation, the significant disregistry along the $\langle 211 \rangle$ direction is consistent with the dissociation mechanism suggested by the dashed slip pathway in Fig. 10b and in Eq. (14). When a stress is applied along the $\langle 111 \rangle$ direction, the dislocation begins to glide across the simulation cell at a critical (Peierls) stress of 0.092 GPa ± 0.007 GPa.
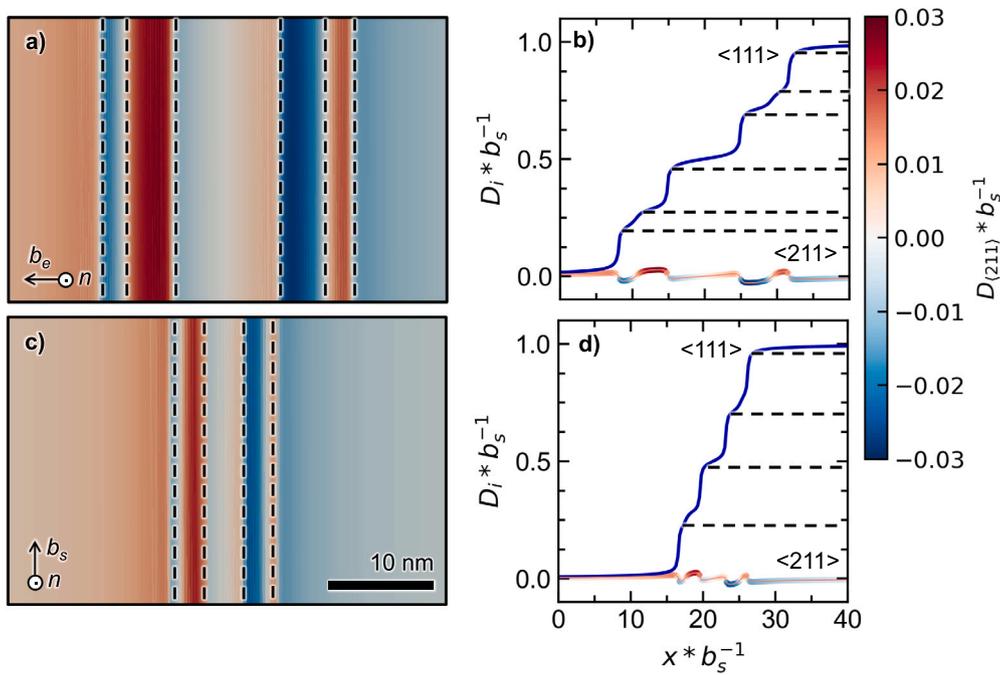
Fig. 11. Visualization of the equilibrium configuration of the [111] (a) edge dislocation core, which is dissociated into 6 partial dislocations indicated by dashed lines (see Eq. (14)) and (c) screw dislocation core, which is dissociated into 4 partial dislocations as indicated by dashed lines (see Eq. (1)). The color coding indicates positive and negative deviation from the [111] slip direction, according to the corresponding color bar. (b,d) Decomposition of the dislocation disregistry into the [111] and [211] directions, across the length of the stacking fault for the edge and screw dislocations, respectively. (For interpretation of the references to color in this figure legend, the reader is referred to the web version of this article.)

A similar investigation applied to the $MnCu_2Al$ screw dislocation in Fig. 11c–d reveals a significant decrease in fault width and a notable change in the dissociation mechanism. Like the equilibrium edge dislocation, the equilibrium screw defect structure predicted by the phase field model has spread into the {110} slip plane, but its total stacking fault width of 9.5 nm (9.5b) is much more compact, yet still regarded as dissociated. In fact, as indicated by Fig. 11c, almost all of the disregistry remains along the $\langle 111 \rangle$ slip direction, and the dissociation of the core appears to be in accordance with the mechanism described by Eq. (1). Schematically, the dissociation of the $\langle 111 \rangle$ screw dislocation follows the pathway suggested by the solid, white line of Fig. 10c. Interestingly, due to the fairly compact nature of this dislocation core, the large jumps in the $\langle 111 \rangle$ disregistry that can be interpreted as partial dislocations bound plateaus in the $\langle 111 \rangle$ disregistry that are short in length. The notion of an *extended* antiphase boundary bounded by $\frac{1}{4}\langle 111 \rangle$ partials is therefore not truly an accurate description of the dissociated $\langle 111 \rangle$ dislocation core. For the screw dislocation, the Peierls stress is 0.220 GPa ± 0.007 GPa.

Under the assumption that there is a small population of defects in the micro-pillar specimen before deformation, the critical resolved shear stress,

$$\tau_{CRSS} = m_{max}\sigma_{YS}, \tag{16}$$

necessary to activate the defects in the micro-pillar experiments is theoretically comparable with the calculated Peierls stresses of the edge and screw defects. Here, σ_{YS} is the yield stress and m_{max} is the maximum Schmid factor within the {110} family of planes for each pillar orientation. In the micro-pillar experiments, τ_{CRSS} ranged from 0.33 GPa to 0.56 GPa. In comparison, the τ_{CRSS} previously measured from bulk single crystals by Umakoshi et al. were 0.40–0.45 GPa [38]. Additionally, nanoindentation at 1 μm depth probes a larger plastic zone of 10 μm [92], and yielded a mean yield stress of 1.02 ± 0.35 GPa (via the Tabor relation), which is within one standard deviation of the mean micro-pillar yield stress from the 5 μm micro-pillars (0.90 GPa ± 0.18 GPa). The potential for micro-pillar size effects on the measured strengths is further evaluated in the Supplemental Information.

The collective evidence suggests that our experiments probed a size regime the reflects a bulk response.

From the phase field model, τ_{edge} and τ_{screw} were found to be 0.092 GPa and 0.220 GPa, respectively. The measured τ_{CRSS} in our investigation are close to the calculated stresses necessary to activate the screw dislocations, assuming that there are additional experimental sources of strengthening that are not accounted for in the simulations, such as mechanisms involving cross slip and dislocation interactions. The closer agreement with the screw stress may indicate that screw dislocation motion controls strength, but further work is needed to test this hypothesis. The defect structures predicted by PFDD, which were $\langle 111 \rangle$-type dislocations that involve dissociation events with splitting widths below the resolution of imaging on an inclined slip plane, are consistent with the TEM and STEM imaging performed on the deformed $MnCu_2Al$ specimen.

5.5. Structure of the planar defects in MnCu₂Al

The atomic stacking sequences within the dissociated core of an edge and screw dislocation are represented schematically in Fig. 12. The results of our phase field model predict that the $MnCu_2Al$ screw dislocation remains fairly compact, but four discrete jumps in the $\langle 111 \rangle$ disregistry do in fact exist—akin to the expected $\frac{1}{4}\langle 111 \rangle$-type partials that have been discussed previously in the literature [37]. However, these multiple partials, each of which are often associated with the formation of extended antiphase boundaries, remain fairly close to one another, prompting the question of whether it is appropriate to designate the region bounded by these partials as an extended antiphase boundary.

The edge dislocation, however, dissociates into six partials that either correspond to $\vec{b}_1$ or $\vec{b}_2$ of Fig. 12. Neither the $\vec{b}_1$ or $\vec{b}_2$ partials shown within Fig. 12c preserve the original stacking sequence, and instead lead to a complex fault, including: complex intrinsic stacking fault (CISF), antiphase boundary (APB), and complex extrinsic stacking fault (CESF) components. The edge dissociation mechanism predicted
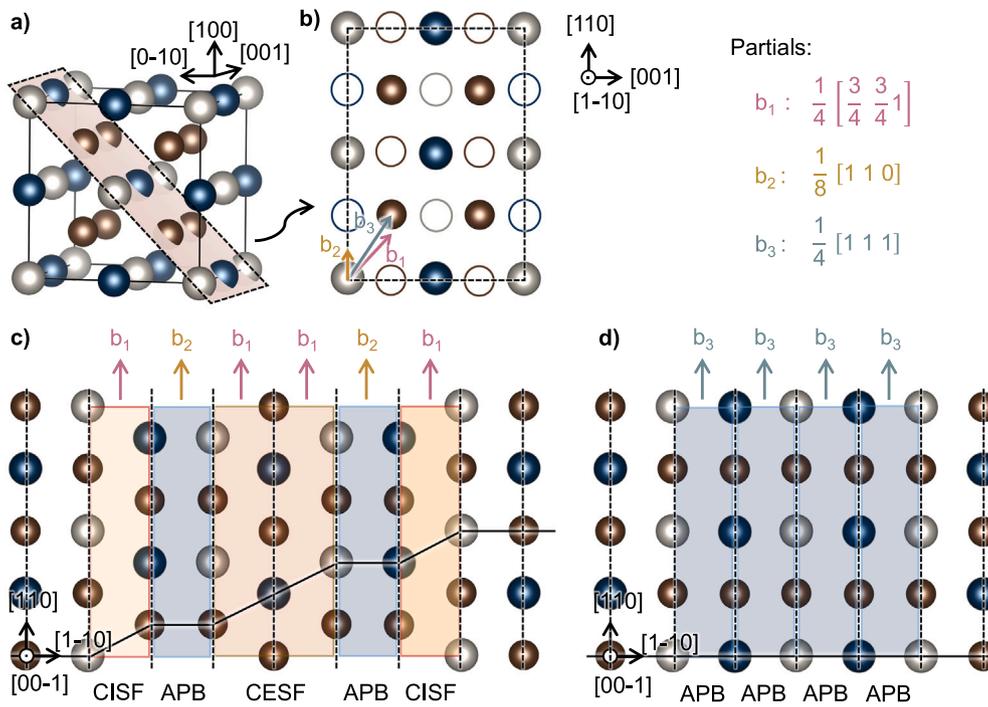
Fig. 12. (a) MnCu$_2$Al Heusler unit cell highlighting the (110) slip plane. (b) The (110) plane indicating partials predicted using the phase field simulations, and c–d the approximate defect structures resulting of the dissociation of the (c) edge and (d) screw defects.

via the phase field model clearly demonstrates that ⟨111⟩ dislocations within the Heusler intermetallic involve an extended, complex dislocation core. As expected, the increased planarity of this dissociated edge dislocation leads to a slightly lower Peierls stress than that of the screw dislocation, implying that they are much more mobile than their screw counterparts. As in other bcc-derived materials [20,75], it is most likely that plastic deformation in MnCu$_2$Al is rate-limited by the less mobile screw defects. However, additional modeling of MnCu$_2$Al defects with mixed character angles and additional characterization of the character angles of the defects present in the deformed specimen is needed to substantiate this observation.

This analysis highlights that the observed complex defect structures in the MnCu$_2$Al Heusler intermetallic mainly arise from the interplay between the electronic structure and elastic anisotropy of MnCu$_2$Al, rather than being solely influenced by crystallographic factors. By analogy to similar analyses conducted on *B*2 intermetallics [20], it is probable that changes in the composition of the Heusler material family will affect the characteristics of defect structures, such as slip direction, dissociation mechanism, fault widths, and Peierls stresses. Our work demonstrates the importance of a robust evaluation of these defect characteristics within material families that exhibit complex core dissociations – including hexagonal close-packed materials, intermetallic compounds, and oxides [20,75] – rather than relying on predictions based solely on the pristine crystal structure.

6. Conclusions

In this study, we explored the deformation and defect structures in the bcc-based Heusler intermetallic through a combination of *in situ* micro-mechanical testing and computational techniques. An *ab initio* informed phase field dislocation dynamics model is developed and used for predicting both defect structures in MnCu$_2$Al, and the minimum stress to move them, at a resolution beyond the current experimental capabilities. Based on our collective findings, the following conclusions can be drawn:

- MnCu$_2$Al exhibits stable plasticity *via* the ⟨111⟩{110} slip family and displays a high degree of elastic anisotropy. No extended antiphase boundaries were observed.
- The number and location of local minima in the {110} γ-surface of MnCu$_2$Al indicate that {110}⟨111⟩ edge dislocations would dissociate into multiple non-collinear partial dislocations rather than the conventionally presumed dissociation into collinear $\frac{1}{4}$⟨111⟩ partial dislocations. In contrast, screw dislocations exhibited the conventional $\frac{1}{4}$⟨111⟩ partial dissociation, though the resulting APB was much more compact than the extended antiphase boundaries that are generally believed to exist in Heusler intermetallics.
- With phase field simulations, we investigate the relaxed core structures of screw and edge dislocations in MnCu$_2$Al by considering the interplay between the γ-surface energies and the elastic interaction between the partials. The results demonstrate that the relaxed cores of the dislocations in MnCu$_2$Al are composed of multiple, closely spaced partials. The fault widths between adjacent partials are narrow, leaving the core much more compact than may be expected of a simpler dissociation producing widely extended antiphase boundaries.
- The predicted planar dislocation core structures and the critical stress to move the screw and edge dislocations can explain the measurable and stable plasticity observed during single crystalline *in situ* micro-compression experiments, and the relatively high yield stresses.

These findings serve to characterize not only the fundamental mechanical properties and elementary characteristics of the complex defect structures within the MnCu$_2$Al Heusler intermetallic, but also highlight the necessity to challenge the prevailing assumption that all defects in bcc-based intermetallics are extended antiphase boundaries. This is of utmost importance, as the dissociation and fault widths of defects in intermetallics have a profound impact on their mechanical – and functional – performance. Ultimately, this understanding paves the way for designing intermetallic precipitate-strengthened materials with enhanced resistance to mechanical duress, particularly in extreme environments.

Declaration of competing interest

The authors declare that they have no known competing financial interests or personal relationships that could have appeared to influence the work reported in this paper.

Acknowledgments

Appendix A. Supplementary data

Supplementary material related to this article can be found online at https://doi.org/10.1016/j.actamat.2024.119711.

References

[1] Z. Li, L. Fu, J. Peng, H. Zheng, X. Ji, Y. Sun, S. Ma, A. Shan, Improving mechanical properties of an FCC high-entropy alloy by γ' and B2 precipitates strengthening, Mater. Charact. 159 (2020) 109989.

[2] M. Kapoor, D. Isheim, G. Ghosh, S. Vaynman, M.E. Fine, Y.-W. Chung, Aging characteristics and mechanical properties of 1600 MPa body-centered cubic Cu and B2-NiAl precipitation-strengthened ferritic steel, Acta Mater. 73 (2014) 56–74.

[3] R. Feng, Y. Rao, C. Liu, X. Xie, D. Yu, Y. Chen, M. Ghazisaeidi, T. Ungar, H. Wang, K. An, et al., Enhancing fatigue life by ductile-transformable multicomponent B2 precipitates in a high-entropy alloy, Nature Commun. 12 (1) (2021) 3588.

[4] T. Yang, Y. Zhao, W. Liu, J. Kai, C. Liu, L1$_2$-strengthened high-entropy alloys for advanced structural applications, J. Mater. Res. 33 (19) (2018) 2983–2997.

[5] A. Suzuki, H. Inui, T.M. Pollock, L1$_2$-strengthened cobalt-base superalloys, Annu. Rev. Mater. Res. 45 (2015) 345–368.

[6] Y. Zhao, T. Yang, Y. Li, L. Fan, B. Han, Z. Jiao, D. Chen, C. Liu, J. Kai, Superior high-temperature properties and deformation-induced planar faults in a novel L1$_2$-strengthened high-entropy alloy, Acta Mater. 188 (2020) 517–527.

[7] G. Song, S.J. Hong, J.K. Lee, S.H. Song, S.H. Hong, K.B. Kim, P.K. Liaw, Optimization of B2/L2$_1$ hierarchical precipitate structure to improve creep resistance of a ferritic Fe-Ni-Al-Cr-Ti superalloy via thermal treatments, Scr. Mater. 161 (2019) 18–22.

[8] W.-C. Lin, Y.-J. Chang, T.-H. Hsu, S. Gorsse, F. Sun, T. Furuhara, A.-C. Yeh, Microstructure and tensile property of a precipitation strengthened high entropy alloy processed by selective laser melting and post heat treatment, Addit. Manuf. 36 (2020) 101601.

[9] S. Wolff-Goodrich, A. Marshal, K.G. Pradeep, G. Dehm, J.M. Schneider, C.H. Liebscher, Combinatorial exploration of B2/L2$_1$ precipitation strengthened AlCrFeNiTi compositionally complex alloys, J. Alloys Compd. 853 (2021) 156111.

[10] Z. Liu, G. Yin, X. Zhu, Q. Zhou, Microstructure, texture and tensile properties as a function of laser power of Ti$_{48}$Al$_2$Cr$_2$Nb$_5$Ta alloy prepared by laser additive manufacturing, J. Manuf. Process. 73 (2022) 624–632.

[11] H. Peng, S. Xie, P. Niu, Z. Zhang, T. Yuan, Z. Ren, X. Wang, Y. Zhao, R. Li, Additive manufacturing of Al$_{0.3}$CoCrFeNi high-entropy alloy by powder feeding laser melting deposition, J. Alloys Compd. 862 (2021) 158286.

[12] Y. Qi, Y. Wu, T. Cao, L. He, F. Jiang, et al., L2$_1$-strengthened face-centered cubic high-entropy alloy with high strength and ductility, Mater. Sci. Eng. A 797 (2020) 140056.

[13] Y. Xiao, X. Peng, T. Fu, L2$_1$-strengthened body-centered-cubic high-entropy alloy with excellent mechanical properties, Intermetallics 145 (2022) 107539.

[14] Y.A. Chang, J.P. Neumann, Thermodynamics and defect structure of intermetallic phases with the B2 (CsCl) structure, Prog. Solid State Chem. 14 (4) (1982) 221–301.

[15] P. Beauchamp, G. Dirras, P. Veyssière, Calculation of antiphase boundaries on {110} planes in a B2 ordered compound by the cluster variation method, Phil. Mag. A 65 (2) (1992) 477–496.

[16] K. Vamsi, T.M. Pollock, A new proximate structure for the APB (111) in L1$_2$ compounds, Scr. Mater. 182 (2020) 38–42.

[17] M.S. Titus, Y.M. Eggeler, A. Suzuki, T.M. Pollock, Creep-induced planar defects in $L1_2$-containing Co- and CoNi-base single-crystal superalloys, Acta Mater. 82 (2015) 530–539.

[18] Y. Eggeler, K. Vamsi, T. Pollock, Precipitate shearing, fault energies, and solute segregation to planar faults in Ni-, CoNi-, and Co-base superalloys, Annu. Rev. Mater. Res. 51 (2021) 209–240.

[19] C. Vailhe, D. Farkas, Shear faults and dislocation core structure simulations in B2 FeAl, Acta Mater. 45 (11) (1997) 4463–4473.

[20] Y.-S. Lin, M. Cak, V. Paidar, V. Vitek, Why is the slip direction different in different B2 alloys? Acta Mater. 60 (3) (2012) 881–888.

[21] Z. Song, H. Hashimoto, C. Chou, H. Endoh, Stacking faults in plastically deformed FeAl alloy with the B2 structure, Phil. Mag. A 64 (2) (1991) 333–339.

[22] F. Heusler, W. Starck, E. Haupt, Magnetisch-chemische studien, Verh. Dtsch. Phys. Ges. 5 (1903) 219–232.

[23] C.S. Birkel, J.E. Douglas, B.R. Lettiere, G. Seward, N. Verma, Y. Zhang, T.M. Pollock, R. Seshadri, G.D. Stucky, Improving the thermoelectric properties of half-Heusler TiNiSn through inclusion of a second full-Heusler phase: microwave preparation and spark plasma sintering of TiNi$_{1+x}$Sn, Phys. Chem. Chem. Phys. 15 (18) (2013) 6990–6997.

[24] J.E. Douglas, C.S. Birkel, N. Verma, V.M. Miller, M.-S. Miao, G.D. Stucky, T.M. Pollock, R. Seshadri, Phase stability and property evolution of biphasic Ti–Ni–Sn alloys for use in thermoelectric applications, J. Appl. Phys. 115 (4) (2014).

[25] T. Graf, C. Felser, S.S. Parkin, Simple rules for the understanding of Heusler compounds, Prog. Solid State Chem. 39 (1) (2011) 1–50.

[26] T. Roy, M.E. Gruner, P. Entel, A. Chakrabarti, Effect of substitution on elastic stability, electronic structure and magnetic property of Ni–Mn based Heusler alloys: An *ab initio* comparison, J. Alloys Compd. 632 (2015) 822–829.

[27] K. Prashanth, H.S. Shahabi, H. Attar, V. Srivastava, N. Ellendt, V. Uhlenwinkel, J. Eckert, S. Scudino, Production of high strength Al$_{85}$Nd$_8$Ni$_5$Co$_2$ alloy by selective laser melting, Addit. Manuf. 6 (2015) 1–5.

[28] H. Jiang, X. Xu, T. Omori, M. Nagasako, J. Ruan, S. Yang, C. Wang, X. Liu, R. Kainuma, Martensitic transformation and shape memory effect at high temperatures in off-stoichiometric Co$_2$VSi Heusler alloys, Mater. Sci. Eng. A 676 (2016) 191–196.

[29] I. Musabirov, I. Safarov, M. Nagimov, I. Sharipov, V. Koledov, A. Mashirov, A. Rudskoi, R. Mulyukov, Fine-grained structure and properties of a Ni$_2$MnIn alloy after a settling plastic deformation, Phys. Solid State 58 (2016) 1605–1610.

[30] W. Maziarz, A. Wójcik, J. Grzegorek, A. Żywczak, P. Czaja, M. Szczerba, J. Dutkiewicz, E. Cesari, Microstructure, magneto-structural transformations and mechanical properties of Ni$_{50}$Mn$_{37.5}$Sn$_{12.5-x}$In$_x$ (x = 0, 2, 4, 6% at.) metamagnetic shape memory alloys sintered by vacuum hot pressing, J. Alloys Compd. 715 (2017) 445–453.

[31] D.H. Dai Hsu, B.C. Hornbuckle, B. Valderrama, F. Barrie, H.B. Henderson, G.B. Thompson, M.V. Manuel, The effect of aluminum additions on the thermal, microstructural, and mechanical behavior of NiTiHf shape memory alloys, J. Alloys Compd. 638 (2015) 67–76.

[32] G.-H. Yu, Y.-L. Xu, Z.-H. Liu, H.-M. Qiu, Z.-Y. Zhu, X.-P. Huang, L.-Q. Pan, Recent progress in Heusler-type magnetic shape memory alloys, Rare Met. 34 (2015) 527–539.

[33] W. Everhart, J. Newkirk, Mechanical properties of Heusler alloys, Heliyon 5 (5) (2019) e01578.

[34] S. Tavares, K. Yang, M.A. Meyers, Heusler alloys: Past, properties, new alloys, and prospects, Prog. Mater. Sci. (2022) 101017.

[35] S. Yang, Y. Kong, Y. Du, L. Shen, Y. Shen, First-principles prediction of structural, mechanical and magnetic properties in Ni$_2$MnAl, Comput. Mater. Sci. 123 (2016) 52–58.

[36] M. Green, C. G.Y., Metall. Trans. (1975) 1118.

[37] M.L. Green, G. Chin, J. Vander Sande, Plastic deformation of single crystals of the Heusler alloy Cu$_2$MnAl, Metall. Trans. A 8 (2) (1977) 353–361.

[38] Y. Umakoshi, M. Yamaguchi, T. Yamane, Deformation and fracture behaviour of the Heusler alloy Cu$_2$MnAl single crystals, Acta Metall. 32 (5) (1984) 649–654.

[39] M. Bouchard, Electron metallography and magnetic properties Cu-Mn-Al Heusler alloys, 1970.

[40] A. Lapworth, J. Jakubovics, Effect of antiphase boundaries on the magnetic properties of Cu-Mn-Al Heusler alloys, Phil. Mag. 29 (2) (1974) 253–273.

[41] B. Dubois, D. Chevereau, Decomposition of the Heusler alloy Cu$_2$MnAl at 360°C, J. Mater. Sci. 14 (10) (1979) 2296–2302.

[42] S. Venkateswaran, N. Nuhfer, M. De Graef, Anti-phase boundaries and magnetic domain structures in Ni$_2$MnGa-type Heusler alloys, Acta Mater. 55 (8) (2007) 2621–2636.

[43] V. Vitek, Structure of dislocation cores in metallic materials and its impact on their plastic behaviour, Prog. Mater. Sci. 36 (1992) 1–27.

[44] J. Schaf, K. Le Dang, P. Veillet, I. Campbell, Extended and local effects of cold work in Heusler alloys, J. Phys. F: Met. Phys. 13 (6) (1983) 1311.

[45] A.A. Coelho, TOPAS and TOPAS-Academic: an optimization program integrating computer algebra and crystallographic objects written in C++, J. Appl. Crystallogr. 51 (1) (2018) 210–218.

[46] F. Crameri, Scientific colour maps, Zenodo 10 (2018).

[47] K. Momma, F. Izumi, VESTA 3 for three-dimensional visualization of crystal, volumetric and morphology data, J. Appl. Crystallogr. 44 (6) (2011) 1272–1276.

[48] F. Bachmann, R. Hielscher, H. Schaeben, Texture analysis with MTEX–free and open source software toolbox, in: Solid State Phenomena, Vol. 160, Trans Tech Publ, 2010, pp. 63–68.

[49] P. Stadelmann, JEMS JAVA electron microscopy software, 2004, http://cimewww.epfl.ch/people/stadelmann/jemsWebSite/jems.html.

[50] W.C. Oliver, G.M. Pharr, An improved technique for determining hardness and elastic modulus using load and displacement sensing indentation experiments, J. Mater. Res. 7 (6) (1992) 1564–1583.

[51] M.P. Echlin, M. Straw, S. Randolph, J. Filevich, T.M. Pollock, The TriBeam system: Femtosecond laser ablation *in situ* SEM, Mater. Charact. 100 (2015) 1–12.

[52] S. Xu, L. Smith, J.R. Mianroodi, A. Hunter, B. Svendsen, I.J. Beyerlein, A comparison of different continuum approaches in modeling mixed-type dislocations in Al, Modelling Simul. Mater. Sci. Eng. 27 (7) (2019) 074004.

[53] L.T. Fey, A. Hunter, I.J. Beyerlein, Phase-field dislocation modeling of cross-slip, J. Mater. Sci. 57 (2022) 10585–10599.

[54] S. Xu, Recent progress in the phase-field dislocation dynamics method, Comput. Mater. Sci. 210 (2022) 111419.

[55] G. Kresse, J. Furthmüller, Efficient iterative schemes for *ab-initio* total-energy calculations using a plane-wave basis set, Phys. Rev. B 54 (1996) 11169.

[56] P.E. Blöchl, Projector augmented-wave method, Phys. Rev. B 50 (1994) 17953.

[57] G. Kresse, D. Joubert, From ultrasoft pseudopotentials to the projector augmented-wave method, Phys. Rev. B 59 (1999) 1758.

[58] J.P. Perdew, K. Burke, M. Ernzerhof, Generalized gradient approximation made simple, Phys. Rev. Lett. 77 (1996) 3865, http://dx.doi.org/10.1103/PhysRevLett.77.3865.

[59] H.J. Monkhorst, J.D. Pack, Special points for Brillouin-zone integrations, Phys. Rev. B 13 (1976) 5188.

[60] J.G. Goiri, A. Van der Ven, MultiShifter: Software to generate structural models of extended two-dimensional defects in 3D and 2D crystals, Comput. Mater. Sci. 191 (2021) 110310.

[61] S. Xu, Y. Su, I.J. Beyerlein, Modeling dislocations with arbitrary character angle in face-centered cubic transition metals using the phase-field dislocation dynamics method with full anisotropic elasticity, Mech. Mater. 139 (2019) 103200.

[62] C. Albrecht, A. Hunter, A. Kumar, I. Beyerlein, A phase field model for dislocations in hexagonal close packed crystals, J. Mech. Phys. Solids 137 (2020) 103823.

[63] H. Kim, A. Zimmerman, I.J. Beyerlein, A. Hunter, Phase field modeling of dislocations and obstacles in InSb, J. Appl. Phys. 132 (2022) 025702.

[64] A.M. Roach, S. Xu, D.J. Luscher, D.S. Gianola, I.J. Beyerlein, Interaction of extended dislocations with nanovoid clusters, Int. J. Plast. (2023) 103684.

[65] S. Xu, J.R. Mianroodi, A. Hunter, B. Svendsen, I.J. Beyerlein, Comparative modeling of the disregistry and Peierls stress for dissociated edge and screw dislocations in Al, Int. J. Plast. 129 (2020) 102689, http://dx.doi.org/10.1016/j.ijplas.2020.102689.

[66] H. Rietveld, Line profiles of neutron powder-diffraction peaks for structure refinement, Acta Crystallogr. 22 (1) (1967) 151–152.

[67] S.-C. Wu, G.H. Fecher, S. Shahab Naghavi, C. Felser, Elastic properties and stability of Heusler compounds: Cubic Co$_2$YZ compounds with L2$_1$ structure, J. Appl. Phys. 125 (8) (2019) 082523.

[68] B. Michelutti, R.P. de La Bathie, E.d.T. de Lacheisserie, A. Waintal, Magnetization, magnetocrystalline anisotropy, magnetostriction and elastic constants of the Heusler alloy: Cu$_2$MnAl, Solid State Commun. 25 (3) (1978) 163–168.

[69] A.K. Zak, W.A. Majid, M.E. Abrishami, R. Yousefi, X-ray analysis of ZnO nanoparticles by Williamson–Hall and size–strain plot methods, Solid State Sci. 13 (1) (2011) 251–256.

[70] A. Materna, P. Haušild, J. Nohava, A numerical investigation of the effect of cubic crystals orientation on the indentation modulus, Acta Phys. Polon. A 128 (4) (2015) 693–696.

[71] J.J. Vlassak, W. Nix, Measuring the elastic properties of anisotropic materials by means of indentation experiments, J. Mech. Phys. Solids 42 (8) (1994) 1223–1245.

[72] A. Datye, L. Li, W. Zhang, Y. Wei, Y. Gao, G.M. Pharr, Extraction of anisotropic mechanical properties from nanoindentation of SiC-6H single crystals, J. Appl. Mech. 83 (9) (2016) 091003.

[73] J. Cahoon, W. Broughton, A. Kutzak, The determination of yield strength from hardness measurements, Metall. Trans. 2 (7) (1971) 1979–1983.

[74] J.S.-L. Gibson, R. Pei, M. Heller, S. Medghalchi, W. Luo, S. Korte-Kerzel, Finding and characterising active slip systems: a short review and tutorial with automation tools, Materials 14 (2) (2021) 407.

[75] F. Wang, G.H. Balbus, S. Xu, Y. Su, J. Shin, P.F. Rottmann, K.E. Knipling, J.-C. Stinville, L.H. Mills, O.N. Senkov, et al., Multiplicity of dislocation pathways in a refractory multiprincipal element alloy, Science 370 (6512) (2020) 95–101.

[76] V. Vitek, V. Paidar, Non-planar dislocation cores: a ubiquitous phenomenon affecting mechanical properties of crystalline materials, Dislocations Solids 14 (2008) 439–514.

[77] L. Liu, L. Chen, Y. Wen, A. Jiang, The structural and elastic properties of a full-Heusler compound Cu$_2$MnAl under pressure, High Temp.–High Press. 49 (4) (2020).

[78] L. Liu, X. Zeng, Q. Gou, Y. Ye, Y. Wen, P. Ou, The structural stability and mechanical properties of Cu$_2$MnAl and Cu$_2$MnIn under pressure: first-principles study, J. Electron. Mater. 47 (2018) 3005–3017.

[79] Y. Wen, X. Zeng, Y. Ye, L. Yan, D. Wu, Q. Gou, L. Liu, First-principles calculations of acoustic and anharmonic properties of ferromagnetic Cu$_2$MnZ (Z=Al and In) Heusler alloys, J. Supercond. Nov. Magn. 31 (6) (2018) 1847–1856.

[80] A. Jain, S.P. Ong, G. Hautier, W. Chen, W.D. Richards, S. Dacek, S. Cholia, D. Gunter, D. Skinner, G. Ceder, et al., Commentary: The Materials Project: A materials genome approach to accelerating materials innovation, APL Mater. 1 (1) (2013) 011002.

[81] J. Jalilian, Comment on 'study of electronic, magnetic, optical and elastic properties of Cu$_2$MnAl a gapless full Heusler compound', J. Alloys Compd. 626 (2015) 277–279.

[82] Ş. Uğur, E. Ulusu, Structural, elastic and electronic properties of Cu$_2$MnZ (Z=Al, Ga, In, Si, Ge, Sn, Sb): A first-principles study, Mach. Technol. Mater. 10 (1) (2016) 39–40.

[83] M. Blackman, On anomalous vibrational spectra, Proc. R. Soc. Lond. Ser. A 164 (916) (1938) 62–79.

[84] A. Every, General closed-form expressions for acoustic waves in elastically anisotropic solids, Phys. Rev. B 22 (4) (1980) 1746.

[85] T. Paszkiewicz, M. Pruchnik, P. Zieliński, Unified description of elastic and acoustic properties of cubic media: elastic instabilities, phase transitions and soft modes, Eur. Phys. J. B 24 (3) (2001) 327–338.

[86] H. Ledbetter, A. Migliori, Elastic-constant systematics in fcc metals, including lanthanides–actinides, Phys. Status Solidi (b) 245 (1) (2008) 44–49.

[87] S. Sandlöbes, M. Friák, S. Zaefferer, A. Dick, S.-b. Yi, D. Letzig, Z.-r. Pei, L.-F. Zhu, J. Neugebauer, D. Raabe, The relation between ductility and stacking fault energies in Mg and Mg–Y alloys, Acta Mater. 60 (6–7) (2012) 3011–3021.

[88] M. Shih, J. Miao, M. Mills, M. Ghazisaeidi, Stacking fault energy in concentrated alloys, Nat. Commun. 12 (1) (2021) 3590.

[89] D. Pettifor, Theoretical predictions of structure and related properties of intermetallics, Mater. Sci. Technol. 8 (4) (1992) 345–349.

[90] J. Bassani, K. Ito, V. Vitek, Complex macroscopic plastic flow arising from non-planar dislocation core structures, Mater. Sci. Eng. A 319 (2001) 97–101.

[91] F.R. Nabarro, M.S. Duesbery, Dislocations in Solids, Elsevier, 2002.

[92] J. Chen, S. Bull, On the relationship between plastic zone radius and maximum depth during nanoindentation, Surf. Coat. Technol. 201 (7) (2006) 4289–4293.